4-8-2020

X-ray Interferometry Without Analyzer for Breast CT Application, a Simulation Study

Jingzhu Xu

X-RAY INTERFEROMETRY WITHOUT ANALYZER FOR BREAST CT APPLICATION, A SIMULATION STUDY

A Dissertation

Submitted to the Graduate Faculty of the
Louisiana State University and
Agriculture and Mechanical College
in partial fulfillment of the
requirements for the degree of
Doctor of Philosophy

in

The Department of Physics and Astronomy

by
Jingzhu Xu
B.S., University of Iowa, 2014
M.S., University of Iowa, 2015
May 2020

ACKNOWLEDGEMENTS

I gratefully acknowledge the funding provided by Louisiana State University Board of Supervisors LIFT2 grant and Board of Regents Proof of Concept grant #LEQSF (2019-20)-RD-D-04, awarded to the principal investigator of this project, Dr. Dey.

I also acknowledge the High-Performance Computing Cluster (HPCC) Facility at Louisiana State University for granting us with CPU-hours for the simulations presented in this study. The content is solely the responsibility of the authors and does not necessarily represent the official views of the funding agencies/institutes for this research.

A special thanks to Professor Leslie G. Butler and Dr. Ham for insightful discussions on the project.

It is a pleasure to thank my advisor Dr. Dey. This dissertation would not be possible without her contribution. It is also a pleasure to thank Dr. Matthews and Dr. Newhauser for providing me with advice and support in academic work.

TABLE OF CONTENTS

LIST OF TABLES

LIST OF FIGURES

ABSTRACT

We investigated a novel analyzer-less X-ray interferometer with a spatially modulated phase-grating (MPG) which produces three types of images (attenuation image, phase image and scatter image) for Breast computed tomography (CT). The system provides the three complimentary X-ray images with the goals of limiting the dose to the object and achieving similar attenuation image sensitivity as a standard absorption-only Breast CT. The MPG system features an X-ray source, a source-grating, a single phase-grating, and a detector. No analyzer grating is necessary, compared to other geometries such as Talbot-Lau X-ray interferometry (TLXI). Thus, there is a ~2 times improvement in X-ray fluence at the detector for our system compared to a same source-detector distance for TLXI, which requires an analyzer grating. In this work we investigated with simulation an MPG Breast CT system to determine if such a system geometry is clinically feasible. First the MPG was conceptually designed and evaluated via Sommerfeld-Rayleigh diffraction integral simulations. Next, we investigated source coherence requirements, fringe visibility, and dependence of phase sensitivity on different system parameters, for a proposed system geometry that should clinically feasible in terms of patient dose. The phase sensitivity of MPG interferometry was proportional to object-detector distance and inversely proportional to the period of broad fringes at the detector, which was determined by grating spatial modulation period. In our simulations, the MPG interferometry achieved 27% fringe visibility for a clinically realistic Breast CT geometry that used a source-detector distance of 950 mm and source-object distance of 500 mm. In conclusion, we simulated a promising analyzer-less X-ray interferometer for Breast CT, which uses a novel spatial sinusoid modulated phase-grating (MPG). Our system is expected to deliver attenuation, phase and scatter images in a single acquisition, with image quality and patient dose that is comparable to general Breast CT.

CHAPTER 1. BACKGROUND AND INTRODUCTION

1.1 Breast Cancer

Mature breast atomically overlays the pectoralis fascia covering major muscle on the chest wall and extends into the axilla. Lobular (milk producing) and ductal (milk carrying) elements, which are embedded in stroma (fibrofatty tissue), compose female adult breast functional glandular tissue [1].

Carcinomas (Adenocarcinomas) are most common breast cancers starting from epithelial cells in the ducts or the lobules. The most breast cancer initiate in the terminal duct lobular units [2]. Based on origin and location of tumor cells, pathologists categorize breast carcinomas into two types: in situ and invasive. Ductal carcinoma in situ (DCIS) means that tumor cells have originated in ducts but not spread into surrounding tissues through the wall of ducts [2, 3]. It largely spreads along ducts in the radial axis of lobular group [2]. Invasive carcinomas, generally including invasive ductal carcinoma (IDC) and invasive lobular carcinoma (ILC), means tumor has broken the boundary of its original tissue and spread into nearby regions, even metastasize to distant organs through the blood or lymph system [2, 4]. It centripetally spreads in the breast stroma from initial invasive location [2].

To determine treatment options, breast cancer staging is used to indicate severity (spread process) of tumor from stage 0 to IV in rank order of carcinoma in situ to metastasis [2, 5]. In consequence, lower number in stage means better or earlier breast cancer. The most used breast cancer staging system is the American Joint Committee on Cancer (AJCC) TNM system [2, 5]. The so-called T categories describe the size of primary tumor. Larger tumor or wider spread gets a higher T number. N and M categories represent tumor's metastasis: N indicates number of lymph nodes involved in tumor (Axillary lymph nodes and supraclavicular lymph nodes are

designated as regional lymph nodes for staging purposes.); M indicates whether distant metastasis happens [2]. When tumor cells disseminate to lymph nodes other than regional ones, metastases are categorized ad distant cases [2]. And bone, lung, brain and liver are the four most common metastatic sites in breast cancers [2, 5].

1.2 Breast Cancer Epidemiology

According to statistics from Centers for Disease Control and Prevention (CDC), breast cancer is the most common cancer and the second highest cause of death among women in the United States. Breast cancer alone accounts for 30% of all the expected new cancer diagnoses and 15% estimated deaths for women in 2020 [6]. Approximately 81% breast cancers are invasive [2]. And 1 in 8 US women will be diagnosed with invasive breast cancer in lifetime [5, 7]. And there are three-quarters of more than 150,000 women living with metastatic breast tumor were originally diagnosed with stage I to III [8]. Five-year relative survival rate of female breast cancers is 90% for early staging, but only to about 22% for stage IV [6, 9].

1.3 Breast Cancer Screening and Diagnosis

To detect breast tumors as early as possible, resulting in more likely successful treatment and improved survival rate, breast cancer screening is recommended for women without any signs or symptoms of breast cancer [5, 10]. Based on American Cancer Society Breast Cancer Screening Guideline, women at average risk for breast cancer should begin to take annual mammography by age 45. For women at high risk of breast cancer, magnetic resonance imaging (MRI) is recommended as well.

When a suspicious site is detected in breast on screening or patients have breast symptoms, breast cancer diagnosis is required. The test and procedure to diagnose breast cancer include diagnostic mammography (may combined with ultrasound), MRI and biopsy.

1.3.1 Mammography

Mammography is a radiographic procedure to detect malignant characteristics, like masses and microcalcifications, in 2D images projected by compressed breasts using low energy X-rays. On mammographic appearance of nonpalpable breast cancer, majority calcifications are associated with DCIS; masses, masses with calcifications and architectural distortion are associated with invasive tumors [11].

However, the screening efficiency of mammography is relatively low for women with high breast density or at high family breast cancer risk [12-14]. In mature female breasts, the relative proportions of fat and fibro-glandular tissue have great individual differences and variations in ages [1]. American College of Radiology Breast Imaging Reporting and Data System (BI-RADS) scales female breast density in four categories: category A are the almost entirely fatty breasts; category B are the breasts with scattered fibro-glandular density tissue areas; category C are the breasts with heterogeneous density, which may blur small masses on mammography; and category D are extremely dense breasts containing 75% or more fibro-glandular tissue [15]. Mammography performs only 60% sensitivity in cases of dense breasts, while it accomplishes a sensitivity of 76% in category A [16, 17]. Moreover, the imaging distortions caused by tissue superposition and breast compression in mammography also result in false-positives and false-negatives in screening exams.

1.3.2 MRI and Ultrasound

MRI is recommended as a screening modality in conjunction with mammography, especially for high risk group. Because it performs high diagnostic sensitivity in any breast density BI-RADS category, whereas has no sensitivity to calcifications [18] and much lower spatial resolution than photon detector in mammography. On the other hand, comparing to screening

mammography which takes 10 to 20 minutes per examination, each MRI examination has more time consumption in 0.5 to 1 hour [18].

Breast Ultrasound, which is generally used in breast cancer diagnosis to evaluate tumor masses, can also be a complementary screening modality combined with mammography to increase sensitivity [18].

1.3.3 Cone Beam Breast CT

Dedicated computed tomography (CT) for breast imaging (Cone Beam Breast CT) is recently developed and some systems FDA approved to represent 3D anatomic structures of uncompressed breasts to overcome limitations of tissue superposition and breast compression in mammography [19-23]. In current clinical based CB Breast CT prototypes at the University of California at Davis (UC Davis) [20-22] and the Koning Corporation (University of Rochester) [23-25], the breasts are scanned by a cone-beam x-ray in pendant geometry when patients lie in the prostrate position on a table with an opening which allows the breasts passing through without compression as Figure 1 (a) shows. And Figure 1 (b) illustrates the implementation of tomography for breasts. The UC Davis prototype provided a high spatial resolution by using the complementary metal oxide semiconductor (CMOS) flat-panel detector, which be able to reach 50 μm pixel size [20-22]. In January 2015, Food and Drug Administration (FDA) approved U Rochester BCT prototype for breast diagnostic imaging in US [24, 25]. Other systems investigate feasibility, flat-panel detectors and spectral optimization for breast CT systems [26-28].

1.4 Multiple Contrast Mechanisms

1.4.1 Attenuation

For conventional radiographic imaging methods, the contrast is generated by differences in X-ray exponential attenuation, which quantifies the probability of a photon particle interacts in

traversed medium. When an X-ray beam penetrates through a medium, absorption via photoelectric effect and scatter via inelastic Compton scattering for incident photons primarily contribute to attenuation. Both these photon particle interactions are the physical foundation of tissue contrast in all conventional radiographic imaging methods [29]. The linear attenuation μ primarily contributes to the contrast mechanism in X-ray while the Compton scatter effect generally introduces bias and reduces contrast. However, due to the fairly small differences in linear attenuation μ for low-Z elements, the contrast between normal breast tissue and tumorous lesion is weak.

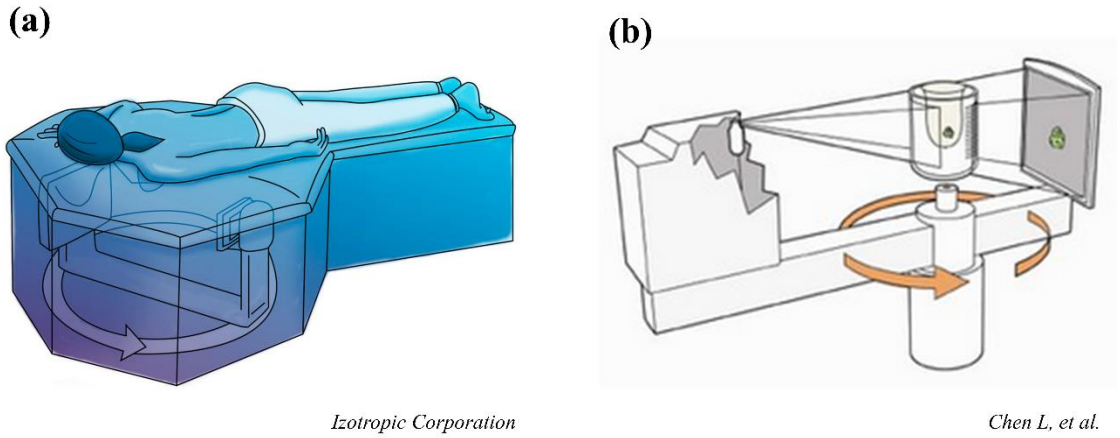

Figure 1.1. Schematic of a dedicated Breast CT. (a) Geometry of CB Breast CT. Breasts are scanned by a cone-beam x-ray in pendant geometry when patients lie in the prostrate position on a table with an opening. (b) An X-ray tube and a flat panel detector rotate around breasts.

1.4.2 Phase Shift

As a result of particle-wave duality, an X-ray photon particle can be also treated as an electromagnetic wave. When an X-ray beam propagates through a medium, a phase shift is induced by refraction and diffraction effects due to X-ray coherent scattering. Figure 1.2 illustrates the contrast mechanism of phase shift. The complex refractive index n quantitatively determines the X-ray phase shift as

$$n = 1 - \delta + i\beta,$$

where δ, the real part of n, is the refractive index decrement corresponding to phase shift and β, the imaginary part of n, responses to X-ray attenuation [18, 30]. The linear attenuation coefficient μ can be related by $\beta = \frac{\lambda}{4\pi}\mu$, where λ is the X-ray wavelength [18, 30]. And X-ray phase shift Φ in medium with the path of transmission can be expressed as $\Phi = \frac{2\pi}{\lambda}\int \delta(s)\, ds$ [18, 30]. For soft tissue composed by low-Z elements, at energy range of radiography, the ratio δ/β is almost 10^3 [30]. For instance, for the tumorous tissue of IDC, δ is about 10^{-6} to 10^{-8}, otherwise β is about 10^{-9} to 10^{-11} in 10 to 100 keV energy range [18]. Consequently, the imaging method based on phase shift substantially has a great potential of increasing soft tissue contrast in radiography.

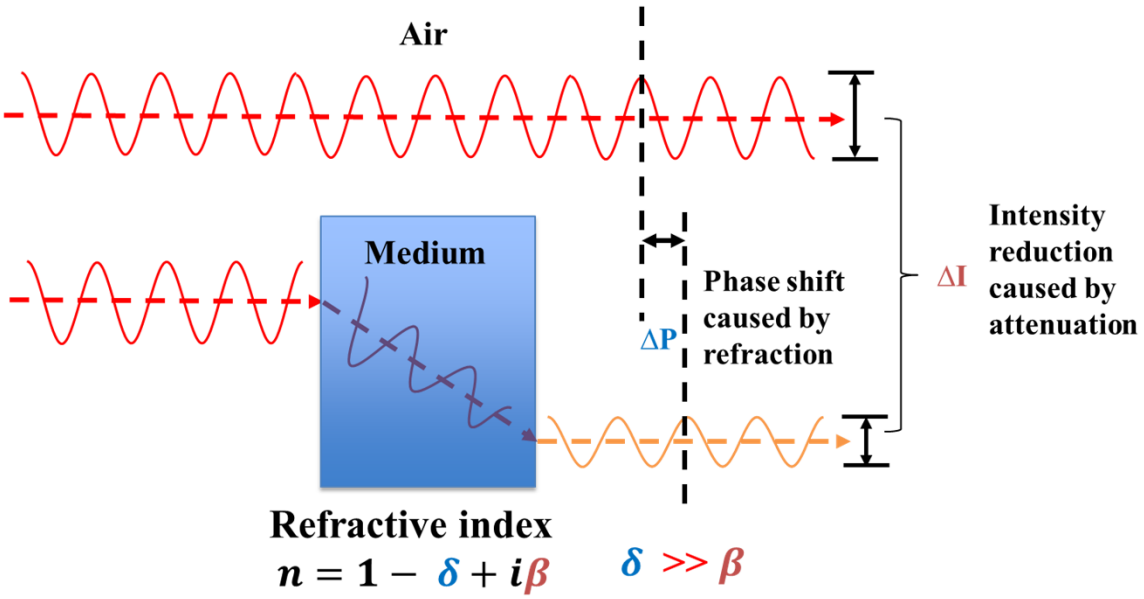

Figure 1.2. Illustration of phase shift contrast due to X-ray refractions.

1.4.3 Small Angle Scatter (SAS)

When an X-ray beam elastically scattered at small angles due to coherent scattering, there is an intensity reduction radially distributed in a small cone shaped region at the incident beam direction [31]. Figure 1.3 illustrates the contrast mechanism of SAS. The premise of intensity reduction is that the X-ray wavelength is much smaller than the scattering scale. In radiographic energy range with short X-ray wavelength (< 0.1 nm), the cross section of SAS mainly depends on scattering events at the scale from 10 nm to 100 μm [32]. As a result, micro-structural variations in medium can be distinguished by contrast due to SAS. And this contrast quantifies differences in nano/micro-scale density in a sample.

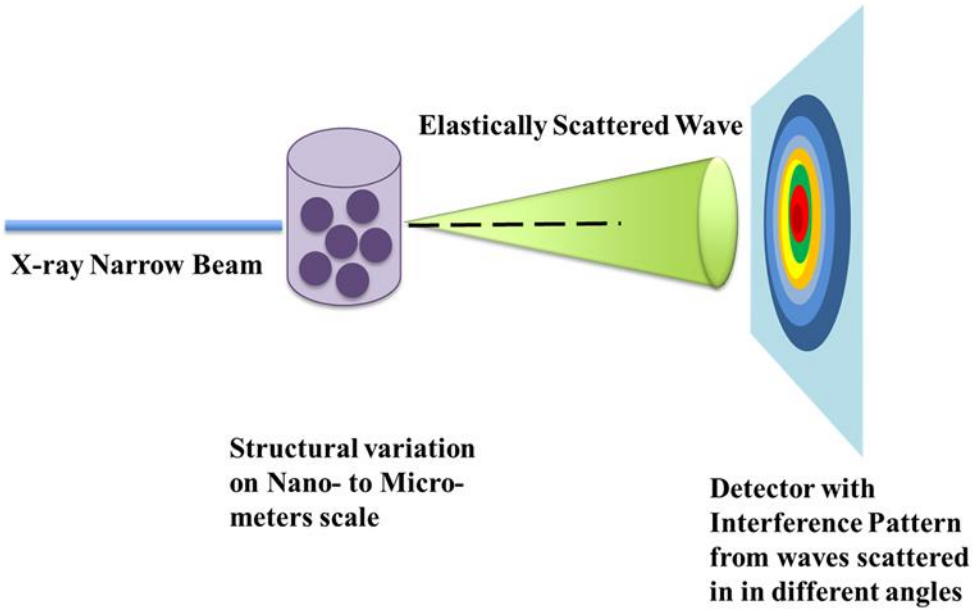

Figure 1.3. Illustration of dark-field contrast due to SAS.

1.5 Grating-based X-ray Interferometry

The X-ray wave properties cannot be acquired by general photon sensitive detectors. The diffraction and interference induced by gratings can convert the wave front distortions from phase shift and SAS into visualized intensity patterns. Within a single exposure, grating-based

interferometry not only provides conventional attenuation information, but also differential phase shift and dark-field (due to SAS) contrast modalities. Therefore, the soft tissue contrast is enhanced by multiple contrast imaging method. The two interferometry methods currently at the forefront are the Talbot-Lau X-ray Interferometry (TLXI) [30, 33-35] and the far-field interferometry by Miao *et al.* [36, 37] from NIH.

1.5.1 Talbot-Lau X-ray Interferometry (TLXI)

Talbot-Lau X-ray Interferometry showed in Figure 1.4 is the most comprehensive pre-clinical grating-based phase sensitive imaging method. A set of linear transmission gratings, phase grating G_1 and analyzer grating G_2, comprises the TLXI. Phase grating G_1 with periodic spatial modulation in phase works as a beam splitter dividing incident X-ray wave front into diffracted beams which will interfere downstream of G_1 and induce periodic fringe intensity pattern by Talbot self-imaging effect [34, 35]. When additional phase shifts due to soft tissues distort X-ray wave front, distortions like translations and deletions also appear on the fringe pattern. Since the phase grating G_1 is made by low-Z materials, like silicon, the photon fluence reduction of phase grating is neglectable [34, 35]. Given extreme short wavelengths of clinical used X-ray, the space between interfered fringes downstream of G_1 at the clinical detectable distance generally is much smaller than spatial resolution of a detector. Therefore, an amplitude grating G_2 with periodic X-ray absorption lines is placed downstream of G_1 ahead of the detector immediately. It works as an analyzer to transform fringe localizations into visualized intensity pattern at detector [34, 35]. The displacement or slight difference between the interference pattern period and G_2 pitch produces broader fringe pattern by Moiré effect [34, 35]. At the same time, the contrast information due to phase shift and SAS from the sample is still reserved un

detectable fringe patterns. Other than phase grating, the analyzer made by high-Z material, like gold, attenuates photon fluence obviously.

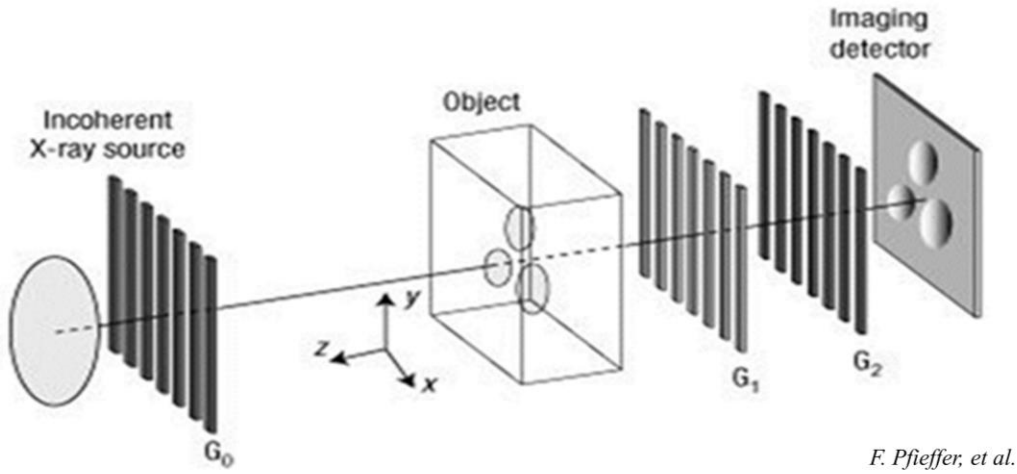

Figure 1.4. Schematic of TLXI [34], including source grating G_0, phasor G_1 and analyzer G_2.

As Figure 1.5 shows, Koehler et al. integrated a Talbot-Lau interferometric unit into the Philips MicroDose L30 multi-slit scanning mammography system to investigate the feasibility of

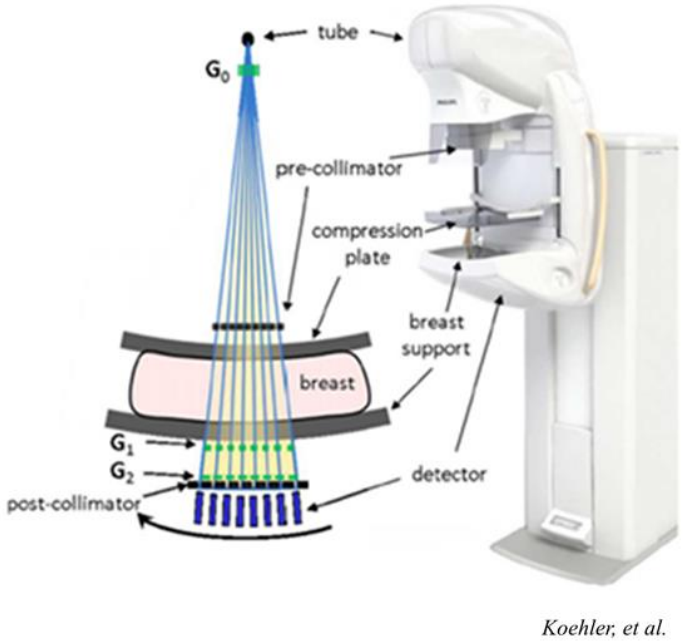

Figure 1.5. Philips MicroDose L30 multi-slit scanning mammography integrated with TLXI.

grating-based multiple contrast imaging method in clinical application [38]. In the standard MicroDose mammography system, the tube with 0.45 mm × 0.65 mm focal spot can work at 26, 29, 32, 35 and 38 kV and the detector pixel is in 50 μm [38]. Different with the conventional mammography system, the tube filter is replaced by the source grating G0 [38]. In the phase prototype geometry, space intervals among the focal spot, G0 and G1 are 100 mm, 510 mm, respectively. The distance of the focal spot to the detector is retained at 660 mm [38]. The space between G1 and G2 is adjustable by the Talbot distance which is determined by the tube energy to obtain maximum fringe contrast. Phase grating G1 is manufactured with pure silicon and absorption lines in grating G0 and G2 are gold. In an experimental scan, a 160 mm × 196 mm FOV took 13s acquisition at 38 kV tube voltage; and the air-kerma was 1.9 mGy approximately [38].

1.5.2 Far-field X-ray Interferometry

Based on the universal Moiré effect, Miao et al. built the far-field x-ray interferometry showed in Figure 1.6 (a) [36, 37]. This eliminated the need for the analyzer by using two (or three) phase-gratings with slight differences in pitch between them to create a low-varying "beat-frequency" (showed in Figure 1.6 (c)) [36, 37]. The ensuing moiré pattern fringes are directly visible with a standard detector (without the analyzer grating), reducing dose about 2-fold [36, 37]. One drawback is that two or three 400 nm phase-gratings are required for that system to obtain fringe patterns [36]. Also, the source-to-detector distance are from 1.7 to 2 m for the *Miao, et al.* systems, which may be challenging to achieve clinically in a hospital setting [36]. The large source-to-detector distance also reduces the fluence at the detector.

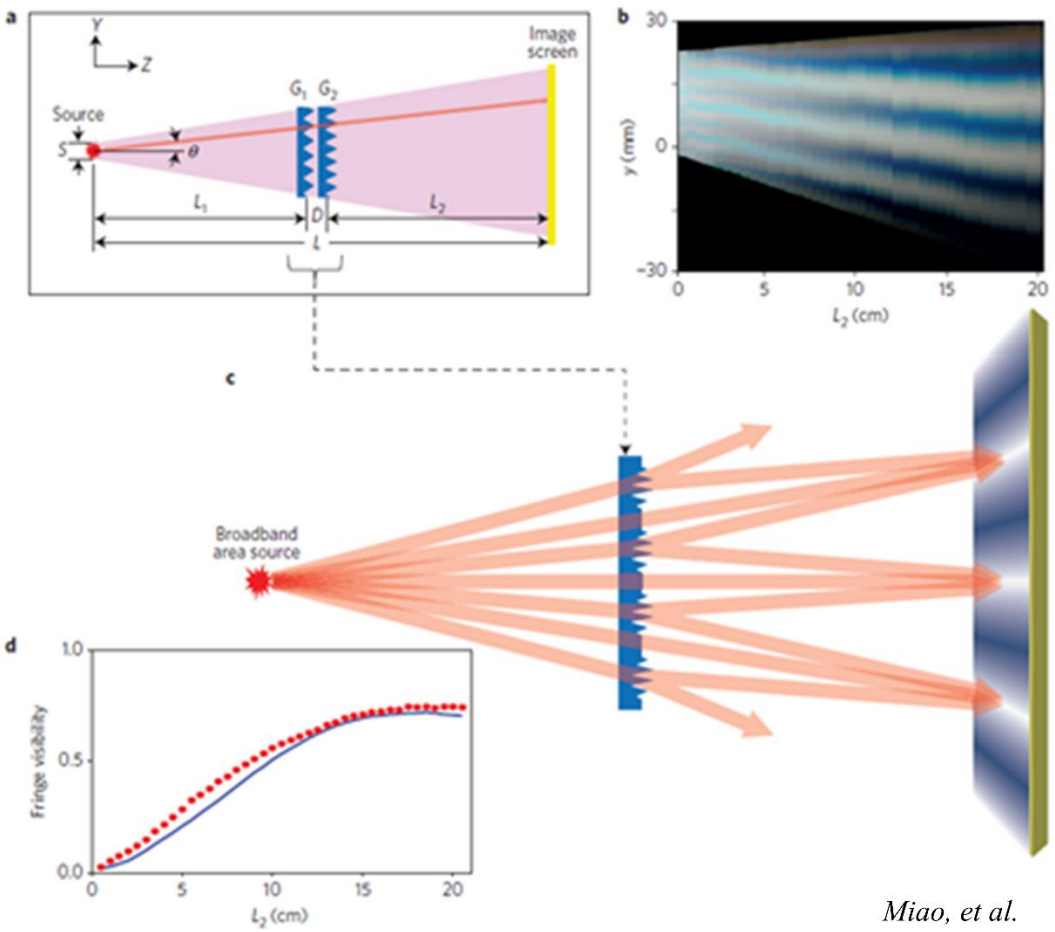

Figure 1.6. Far field dual phase grating interferometry reproduced from *Miao, et al.* [36, 37]. (a) Schematic of geometry setup. (b) Detectable fringe pattern by phase Moiré effect along beam propagation direction. (c) Illustration fringe pattern created by a low-varying "beat-frequency". (d) Fringe visibility vs. the space between phase grating G_1 and G_2.

1.6 Motivation

Although dedicated Breast CT overcomes the limitations of tissue superposition and alteration of geometric structure due to compression, and improves low sensitivity for dense breasts, the diagnostic sensitivity of Breast CT for breast cancer is still limited by low soft tissue contrast due to attenuation. Interferometry, providing phase contrast and dark field contrast, has the potential to perform better than Breast CT for breast cancer diagnosis. Phase contrast has

much higher detector sensitivity than attenuation [18, 30]. Dark field contrast due to X-ray SAS has potential to detect microcalcification clusters in breast tumors [32]. Therefore, multiple contrast imaging method by X-ray interferometry is a feasible option to improve diagnostic sensitivity of breast cancers.

Recently, TLXI has shown the potential to improve detection accuracy of mammography [39-41] and micro-calcification classification [41, 42] helping detection and early-diagnosis. Phase images identified trifocal tumors where X-ray absorption images failed [39]. Complementary information from absorption and scatter images [42] distinguished oxalate vs. hydroxyapatite micro-calcifications, providing a non-invasive scoring of malignancy or pre-malignancy-risk. While TLXI has made the most clinical stride in the mammogram domain [18, 38, 41-44], an absorption grating (analyzer) is needed to see interference patterns with standard cost-effective X-ray detectors, which is detrimental from dose/fluence consideration.

For a variety of reasons, such as dose, cost, complex geometry, and bulkiness, many X-ray interferometer systems described in the literature fall short of clinical compatibility. Given that the analyzer reduces the photon fluence at detector by nearly half, TLXI is not a clinical compatible multiple contrast imaging method. If the incident photon fluence is increased to get same image qualities as general Breast CT, the increase in dose-to-patient is also inevitable. The other X-ray interferometry methods have limits in geometry, like the far field interferometry by *Miao, et al.* [36, 37], and monochromatic X-ray source. Considering clinical compatibility, a near field X-ray phase grating-based interferometry is preferred.

Our eventual goal is to build a multiple contrast Breast CT system, yielding similar quality attenuation images, while also providing phase and scatter images without increasing the dose to patient. Towards this goal we show a potential design in simulations, where we find a feasible

system geometry and the grating parameters and address critical issues like effects of source coherence, source-spectrum on fringe-visibility, focal-spot, phase-sensitivity etc.

1.7 Hypothesis and Specific Aims

The clinical compatible multiple contrast Breast CT with novel X-ray interferometry method will acquire multiple contrast image modalities by an analyzer-less X-ray interferometry geometry to preserve image quality while simultaneously keeping radiation dose to a reasonable level. The novel X-ray interferometry geometry is well suited for adaptation into the same footprint as current clinical Breast CT prototypes, including X-ray source, geometry and data acquisition workflow.

Specific Aim 1 investigates the spatial structure of modulated phase gratings. An MPG must modulate an incident monochromatic X-ray plane wave into a periodic fringe pattern at the detector, which must be located at a clinically compatible distance. The design parameters of an MPG are investigated to find a design that provides the best fringe visibility.

Specific Aim 2 models a clinically compatible multiple contrast Breast CT imaging system based on X-ray interferometry with an MPG. The requirements imposed on various design choices, such as source coherence, are investigated. The MPG interferometry components are integrated with an X-ray source and acquisition geometry that matches those typically used in cone beam Breast CT systems.

Specific Aim 3 simulates the forward projections of simple objects (like spheres and gradient wedges made of different materials) as scanned by the multiple contrast Breast CT imaging system described in Specific Aim 2. From the simulated projections, absorption, phase contrast and dark field images are retrieved. The imaging sensitivity of phase shift and SAS in the novel grating-based interferometry is analyzed quantitatively.

CHAPTER 2. METHODS

2.1 Optical Simulation

To demonstrate the operation of such a system, we simulated a system shown in Figure 2.1 using the Sommerfeld-Rayleigh diffraction integral (SRDI) [45, 46]. The X-ray transmission function through a phase grating in a plane perpendicular to the X-ray incidence direction on the z axis is defined as

$$T(x\,, y) = A(x\,, y)e^{j\phi(x,\ y)} \tag{1}$$

where $\phi(x,\ y)$ is the z projection phase shift determined by grating spatial structure and $A(x,\ y)$ is the corresponding amplitude transmission due to attenuation of X-rays.

The amplitude of the diffracted X-ray wave at the detector is obtained by evaluating the SRDI formula for the Huygens-Fresnel principle. In Figure 2.1, $D_{sg} = z_1 - z_0$ denotes the distance between source and grating on the z axis. $D_{gd} = z_2 - z_1$ denotes the distance between grating and detector on the z axis. According to the Sommerfeld-Rayleigh diffraction integral, the amplitude of the X-ray on the detector plane is

$$\boldsymbol{A}(x_2, y_2, z_2) = \frac{1}{j\lambda}\iint U(P_s)\cdot\frac{e^{jkr_0}}{r_0}\cdot T(x_1, y_1, z_1)\cdot\frac{e^{jkr_1}}{r_1}\cdot\cos\theta\, dx_1 dy_1 \tag{2}$$

and the intensity is

$$\boldsymbol{I}(x_2, y_2, z_2) = |\boldsymbol{A}(x_2, y_2, z_2)|^2 \tag{3}$$

where $k = \frac{2\pi}{\lambda}$ is the wave number and λ is the wavelength, $U(P_s)$ is the X-ray source wave function at (x_0, y_0, z_0) , r_0 is the distance between source and point (x_1, y, z_1) on the grating given by $r_0 = \sqrt{{D_{sg}}^2 + (x_1 - x_0)^2 + (y_1 - y_0)^2}$ and r_1 is the distance between grating point (x_1, y_1, z_1) to detector point (x_2, y_2, z_2) given by $r_1 = \sqrt{{D_{gd}}^2 + (x_2 - x_1)^2 + (y_2 - y_1)^2}$, and θ

is the angle between $\overrightarrow{r_1}$ and the normal to the plane of grating. The $\cos\theta$ term is also given by $\cos\theta = \frac{D_{gd}}{r_1}$.

In the initial stage of design, the source wave function $U(P_s)$ is assumed as a parallel beam of X-rays. Therefore, Eq. (2) can be simplified as

$$\boldsymbol{A}(x_2, y_2, z_2) \propto \frac{D_{gd}}{j\lambda} \iint T(x_1, y_1, z_1) \cdot \frac{e^{jkr_1}}{{r_1}^2} dx_1 dy_1 \quad (4)$$

where we consider a planar wave incident on grating. Since the distance of plane wave to grating is assumed to be infinity, we can ignore that term. We replaced the $\cos\theta$ (between the r_1 and z-axis) by $\frac{D_{gd}}{r_1}$, resulting in a r_1^2 term appearing in the integral in Eq. (4). When displaying intensity carpet, we show the normalized intensities at each D_{gd} to better visualize the fringe-visibility.

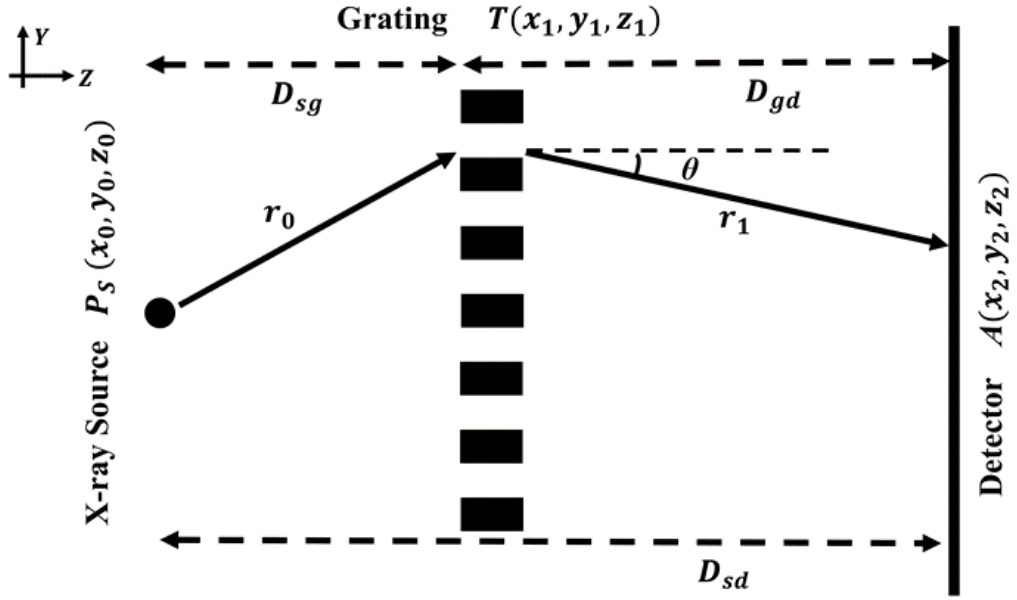

Figure 2.1. Schematic system diagram of SRDI, including a point source, grating and detector.

To verify our computation, we simulated the Talbot carpet (Figure 2.2) for the Talbot-Lau system for a 4 μm standard G_1 phase grating that is typically used in the TLXI system [34, 35].

We cover distances of 0 to 200 mm from grating. The pattern is as expected for the π-shift grating and we observe the first and third Talbot distances at correct distances of 40.3 mm and 120.9 mm respectively [35]. We note that the fringe pattern periodicity is only about 4 μm and hence an analyzer (absorption grating) is required to observe patterns on a typical clinical X-ray detector (35-75 μm pixel size).

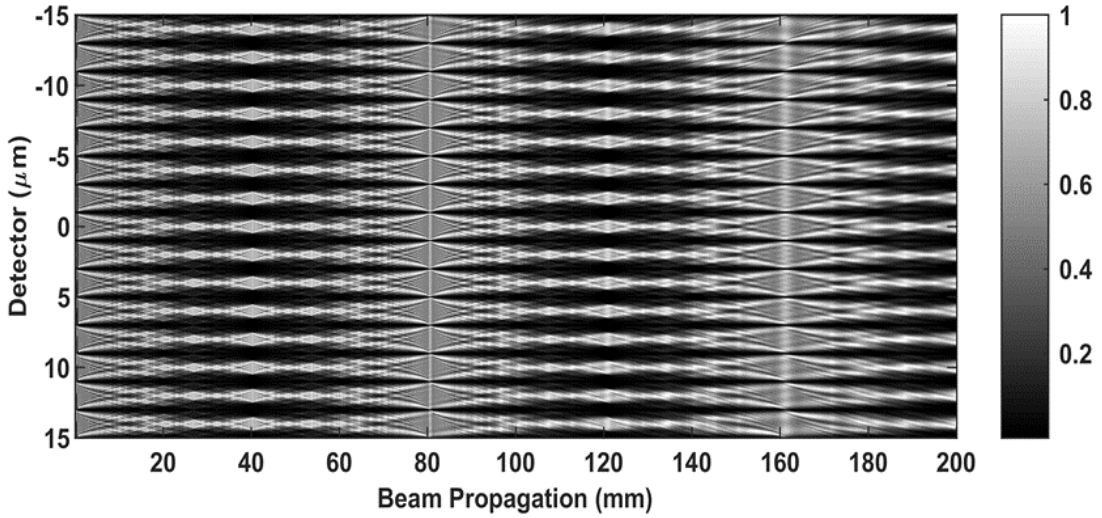

Figure 2.2. Normalized talbot-carpet for a 4 μm π-phase-grating typically used in Talbot-Lau interferometer. The first and third order Talbot-distances from the grating are 40.3 mm and 120.9 mm.

2.2 Specifications of the Cone Beam Breast CT Prototypes

Based on current developed Breast CT prototypes, including UC Davis, U Rochester and U Naples which built up with a high-solution detector and microfocus X-ray source, a cone beam X-ray source and a flat-panel detector rotate around breast circularly or spirally by a rotation gantry or a slip ring [19-27]. For cone beam X-ray sources, the energy spectrum is determined by 40 to 60 kV tube voltage with 0.2 to 0.3 mm Cu filter [20, 22, 24]. Except the microfocus source, the focal spot of X-ray sources is in 0.1 to 0.3 mm [20, 22, 24]. For TFT or CMOS flat-panel detectors with CsI:Tl scintillator, pixel pitches varies in 50 to 200 μm [20, 22, 24]. For geometry,

the distance from source to isocenter is about 50 to 65 cm with 1.4 to 2 magnification factors [20, 22, 24]. The breast containers dimension is generally in 30×30×40 cm [20, 22, 24]. For the study of multiple contrast imaging, X-ray interferometry is required to be coupled in current clinical used Cone Beam Breast CT prototype. Table 2.1. outlines specifications of multiple contrast Breast CT used in simulations and the geometric setup is showed in Figure 2.3.

2.3 Phase Grating Design

As shown in Figure 2.2, without the analyzer, the intervals of intensity fringes are much smaller than the pixel size of a typical high resolution flat-panel detector (50 μm), making the fringe pattern impossible to be distinguished. As a result, there will only be a bright spot displayed on the detector. Figure. 2.4 shows this phenomenon in simulations; Figure 2.4 (a) is the 1 μm pitch

Table 2.1. Specifications of multiple contrast Breast CT

		Parameters
X-ray Source	Focal Spot Size (mm)	0.3
	Tube Voltage (kV)	60
	Filter (mm)	0.2 Cu
Flat-panel Detector	Type	CMOS
	Pixel Size (μm)	50
Geometry	Source to Isocenter (cm)	50
	Isocenter to Detector (cm)	45
	Magnification Factor	1.9

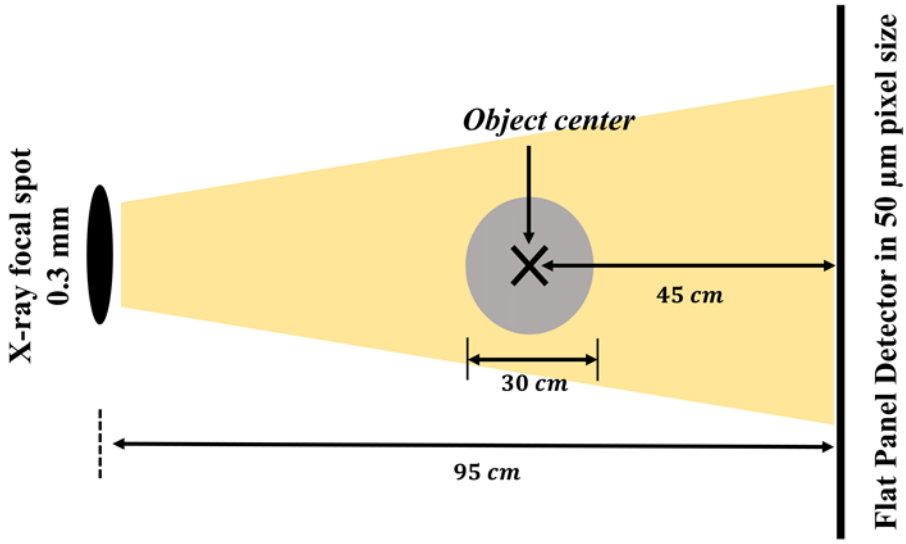

Figure 2.3. The Breast CT geometry applied in simulations of multiple contrast imaging method.

grating spatial structure with a 10 μm aperture, Figure 2.4 (b) is the intensity pattern in high resolution and Figure 2.4 (c) is the intensity smoothed with a 5 μm box filter. The plot is shown in original resolution for ease of comparison.

2.3.1 Effect of phase-shift to intensity modulation

The X-ray interference pattern induced from a phase grating which has a multiple-slit structure is modulated by phase modulation of grating. Periods of interference fringes vary for difference phase modulations in phase gratings. And at a typical grating-to-detector distance, interference stripes have different resolutions due to different phase-grating phase-shifts. Figure 2.5 shows different X-ray interference patterns induced by a multiple-slit phase grating in 4 μm pitch with different phase shift at 20 keV. In Figure 2.5 (a) to (d), the phase-shifts are $\pi/4$, $\pi/3$, $\pi/2$ and π. Misalignment and mergence among interference stripes from difference phase modulations can be used to shape intensity pattern at detector.

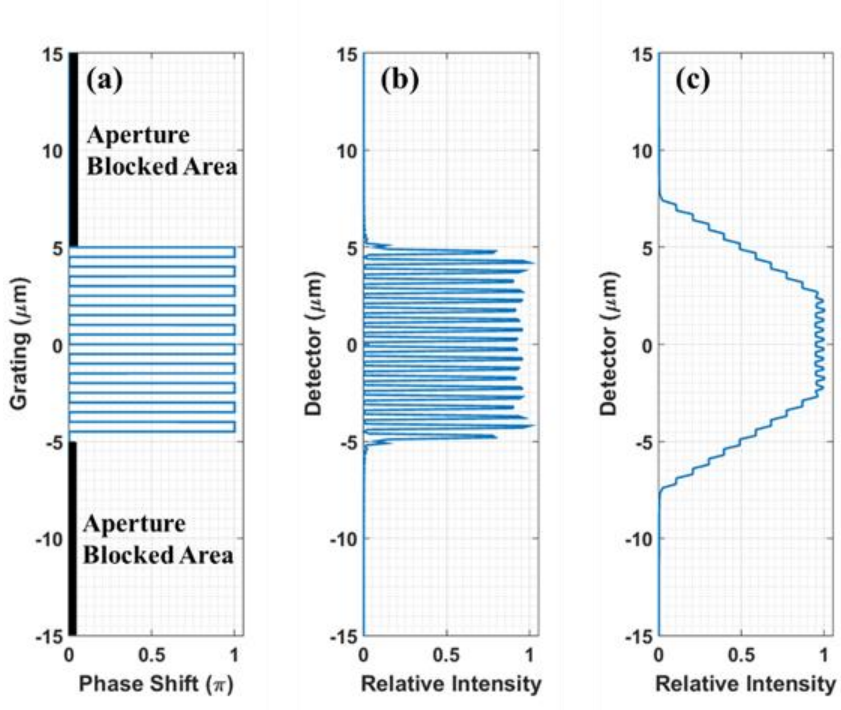

Figure 2.4. Intensity pattern without analyzer in low resolution detector. (a) Spatial structure of a phase grating with aperture. Pitch width is 1 μm and aperture open width is 10 μm. (b) Normalized intensity with high resolution (0.1 μm pixel size) at the first order Talbot distance 2.5 mm downstream of the grating with 25 keV X-ray. (c) Normalized intensity after convolving with a 5 μm width window function.

2.3.2 Sinusoidal Modulated Phase Grating (MPG)

The amount of phase shift modulation from grating is determined by the phase-shift or the height of the grating. A grating with a different phase shift produces spots with different brightness for the same grating-to-detector distance. To demonstrate this point, two gratings (inside same structure) with different heights (phase shifts) are placed adjacently as Figure 2.6 (a); then, intensities of the two individual gratings and the intensity of the combined grating are shown in Figure 2.6 (b). Broad fringes composed by different bright spots distributed at regular intervals can then be created by repeating the lower- and higher- level combined phase grating units on the plane perpendicular to the optical axis. Figure 2.7 shows an entire fringe pattern created by this method. The period of broad fringe pattern can be controlled by the width of

multiple-slits. A spot with high brightness is the crest of a fringe and adjacent spots with lower brightness are the trough. In Figure 2.6 and 2.7, the X-ray energy is 25 keV, grating to detector distance is 300 mm. The grating function is sampled at 1 nm and the detector is sampled at 10 nm.

To demonstrate the concept of the phase grating design, a rectangular-pattern grating was useful (Figure 2.4, 2.6 and 2.7), but better fringe-visibility is obtained from a sinusoidal pattern, such as shown in Figure 2.8, where the superposing structure is a sinusoidal. The sinusoidal was chosen as it has no sharp cut off and is expected to yield better fringe visibility and other system characteristics. Also, it can be approximated as a triangular modulation of the grating. In conference presentations, we have demonstrated in simulations for MPG with either rectangular modulation or truncated quadratic modulations [47, 48]. In what follows, we assume a sinusoidal pattern to compute our carpets and visibility.

In a very different concept, for TLXI, “saw-tooth” grating elements were used instead of standard “binary” grating improving contrast and compactness [49]. This is physically and functionally different from our MPG case. For the MPG case, the height of the elements is slow-varying in a given functional form (such as a sinusoid), while in the TLXI work with saw-tooth grating, the grating structure does not have a height changing modulation of a base grating and will require an analyzer for imaging with standard X-ray detectors [32].

We also note that the proposed system is *physically and functionally* distinct from another analyzer-less system [36, 37] by Miao, et al. Our system uses a single phase-grating with modulated structures (MPG) while the system [36, 37] by Miao, et al. used three gratings with standard structure (i.e. without modulation). Functionally, the MPG versus multiple standard-

phase-gratings makes our system compact (< 1m) compared to the Miao et al system (~2 m), which makes our system clinically feasible.

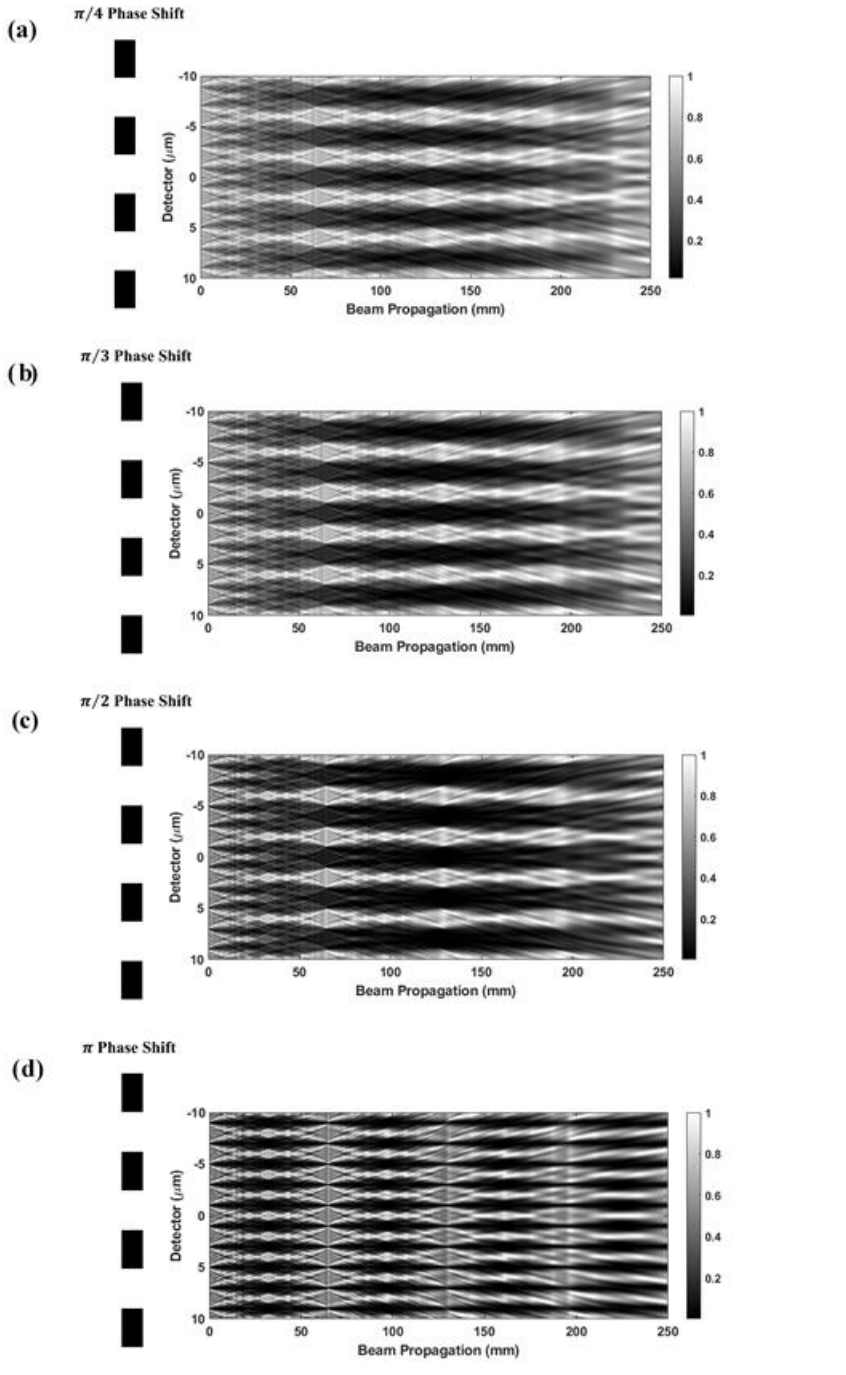

Figure 2.5. Effect of phase shift for intensity modulation. (a) Grating with $\pi/4$ phase shift. (b) Grating with $\pi/3$ phase shift. (c) Grating with $\pi/2$ phase shift. (d) Grating with π phase shift.

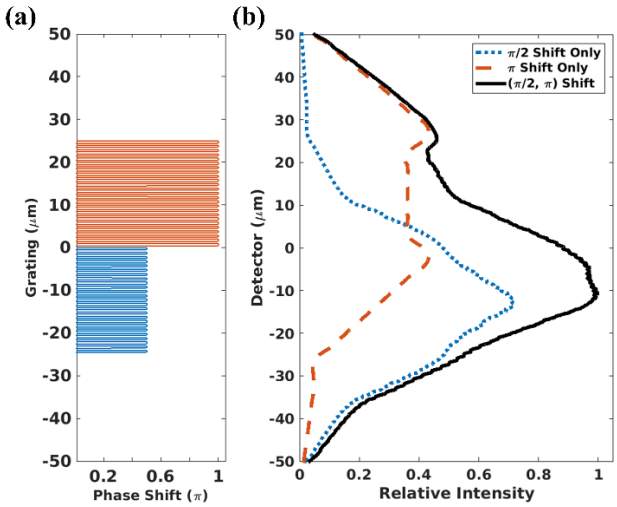

Figure 2.6. A grating with a different phase shift. (a) Spatial structure of a grating combined by two linear gratings with π/2 and π phase shifts with 1 μm pitch. (b) Normalized intensities at 30 cm downstream of the grating with 25 keV X-ray. The red and blue dashed lines show the intensity of response due to the individual gratings (π shifter in blue and π/2 shifter in red).

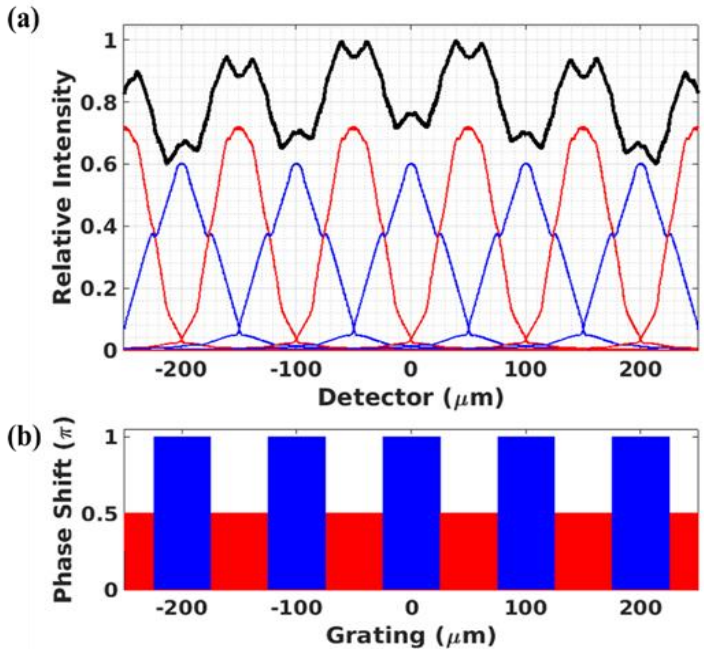

Figure 2.7. A grating with repeated lower- and higher- level combined phase units. (a) The entire fringe pattern (black curve) due to repeated units of low-high linear phase shift grating combination. The red and blue curve indicates individual wave front intensities modulated by the grating units at π/2 and π respectively shown in (b). (b) The entire grating is plotted to show corresponding alignment of grating units. Here, the pitch period is 1 μm, X-ray energy is 25 keV, grating to detector distance is 300 mm and the high-low pattern is repeated at 100 μm (W = 100μm).

2.4 Performance Simulations of Our System

We performed a series of simulations for our system with increasing complexity, beginning with (1) the intensity carpet and fringe visibility analysis along the z-direction with a parallel source at 40 keV. The MPG-to-detector distances are varied as $z = 450\ to\ 750$ mm. We also analyzed the dependence of fringe visibility on energy, pitch and grating spatial modulation period W, at different MPG-to-detector distances. (2) The intensity carpet with a point source at 40 keV and 250 mm source-to-MPG distance is shown. Degradation of visibility due to polychromatic point source with a typical spectrum for Breast CT is shown. (3) We compute the spatial coherence requirement and show the fringes and fringe visibility for a line-source compared to a point source. Each of these are explained in more detail below.

2.4.1 Intensity carpet and fringe analysis with mono-energetic, parallel source

A carpet for Talbot-Lau phase-grating such as one shown in Figure 2.2 captures the intensity of the interference pattern at different distances from the grating and is useful for determining optimal detector placement. We considered the spatial modulated phase grating (MPG) (Figure 2.8) with phase heights $(h_1, h_2) = (\pi/4\,, \pi)$, 0.6 to 1.2 μm pitch and 100 to 200 μm W. For parallel source, the source-to-grating distance is assumed as infinite, thus, there is no magnification from geometry, or the fringe period $W' = W$.

We computed the fringe-intensity carpet for our grating pattern with 100 μm W at 450 to 750 mm MPG-to-detector distance. A mono-energetic (40 keV) parallel source is assumed. The grating is sampled at 1 nm and the detectors (at each z) are sampled at 10 nm. We consider detector placement in the beam propagation direction z with 5 mm intervals. We show the carpet with two cases of pitch, 1 μm and 0.6 μm. And the visibility around the central axis is also calculated by

$\frac{I_{peak} - I_{trough}}{(I_{peak} + I_{trough})} \times 100\%$ at every placement and plotted with respect to z, where the I_{peak} and I_{trough} are the intensities at the peak and trough of the fringes, respectively.

For the same geometry, the fringe visibilities at 450 to 750 mm MPG-to-detector distances are computed and plotted for different energies between 20-50 keV, different grating pitches between 0.6-1.2 μm and different fringe periods between 100-200 μm. These analyses allow for other system design considerations (low energy mammogram to higher energy CT).

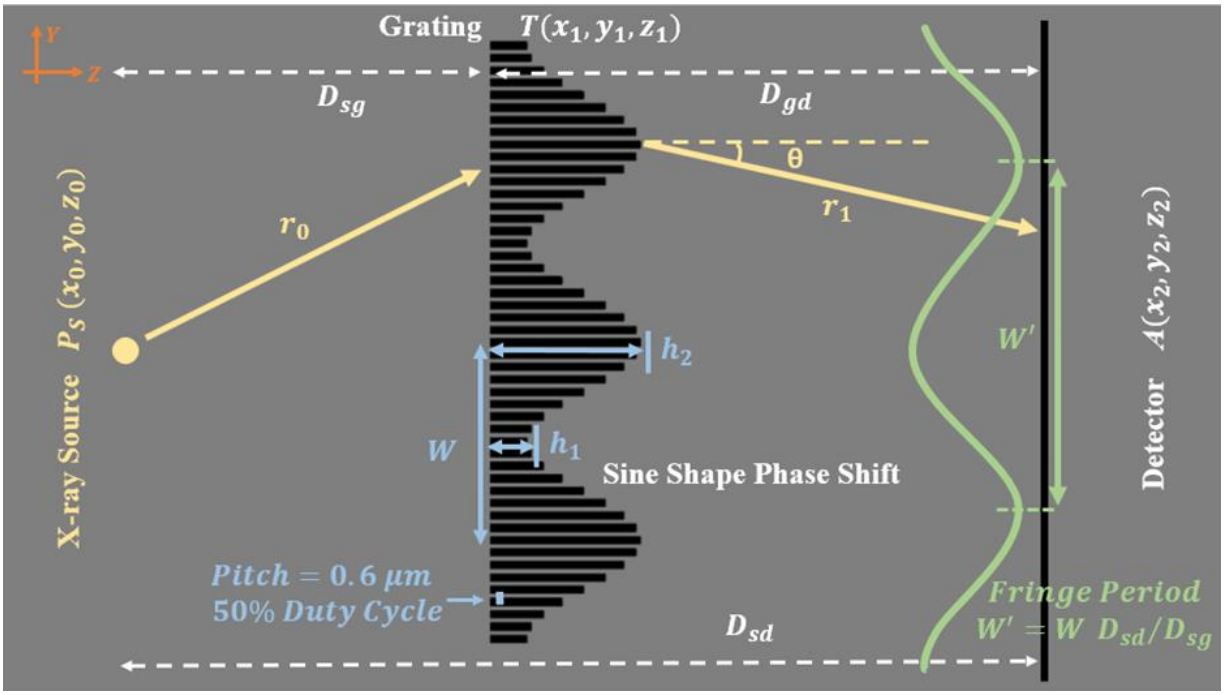

Figure 2.8. Schematic system diagram (NOT TO SCALE): source, grating and detector. The source is simplified to a point source here but in reality, there is an X-ray tube and source-grating (with composite line sources). The grating-to-detector distance D_{gd} can be 45-75 cm making it a compact system with source-to-detector distance D_{sd} of ~ 1 m. The grating is a special one with a sinusoidal modulation of period W over a structure of (smaller) pitch P. The heights h_1 and h_2 are the heights presented to the X-ray beam to shift the phase by certain amount (ex. π/4 and π) for the center-wavelength. Through geometric magnification D_{sd}/D_{sg} of W, broad sinusoidal fringes with period W' are displayed on the detector.

2.4.2 Fringe analysis with a monochromatic and polychromatic point source

Point Source Carpet, monoenergetic: We simulated the intensity with a monochromatic (40keV) point source for a source-to-MPG distance of 250 mm and MPG-to-detector distance varying from 450 to 750 mm. For a spherical wave from the point source in the cone-beam geometry, the fringe period W' on the detector is the grating spatial modulation parameter W scaled by magnification factor D_{sd}/D_{sg} (see Figure 2.8).

Temporal Coherence: To demonstrate that MPG can work well with broad energy band like TLXI and propagation-based interferometers [34, 35], we simulated the fringe intensities with a point source in the range of 26 to 60 keV individually for a given MPG with fixed phase heights $(h_1, h_2) = (\pi/4\,, \pi)$ at 40 keV. With the geometry of a source-to-MPG distance $D_{sg} = 250$ mm and an MPG-to-detector distance of $D_{gd} = 600$ mm, the visibility of 150 μm periodic fringes for each energy were computed and showed in the results section.

Point Source, poly-energetic (Breast CT Spectra): For a given MPG-to-detector distance of 600 mm and source-to-MPG 250 mm, we compare the fringes at the detector from a monochromatic source versus a polychromatic spectrum suitable for Breast CT. For example, for the UC Davis prototypes of Breast CT, the spectrum is set up by 60 kV with 0.2 mm Cu filter [20, 22]. The X-ray source is an aggregate of sources with different energies each weighted by the number of photons at the typical energy in the spectrum. The sources of different energies are incoherent and responses to all the weighted sources are added in intensity [35, 50].

2.4.3 Spatial coherence requirement and source grating

We now consider two issues: one is the spatial coherence requirement of source for interference fringes to occur for our system and second is the effect of the focal spot blur. These concepts are similar to TLXI and have been analyzed in depth for TLXI [28, 33] and we go over them briefly

for our system. X-ray tubes typically used for clinical Breast CT or Mammogram are in-coherent sources. We therefore require a source grating G_0 such as required of the TLXI system. G_0 is placed close to the X-ray tube focal spot. It can be thought of series of line sources of length L_s, which are mutually in-coherent [34, 35].

For a single line source of size L_s, the corresponding projected source size $L_s \frac{D_{gd}}{D_{sg}}$ on the detector will be convolved with the fringe intensity profile from a point source. Since the broad fringe (> 50 μm) created by MPG is composited by super fine fringes (in the order of grating pitch) with sinusoidal intensity modulation of W' (> 50 μm), the degradation of visibility (due to the convolution of a line source projection, assumed as a window function, with the finite size which is smaller than one pixel size of 50 μm) will be low.

For our geometry, when $L_s \frac{D_{gd}}{D_{sg}} \leq 50\ \mu m$, the line source size $L_s \leq 16.6\ \mu m$, where D_{sg} is the distance from source grating G_0 to MPG and D_{gd} is the distance from MPG to detector. However, the coherence length for the peak-wavelength is given by

$$l_c = \frac{\lambda D_{sg}}{P_0 \Upsilon_0} = \frac{\lambda D_{sg}}{L_s} \tag{5}$$

where λ is the peak-wavelength, P_0 and Υ_0 are the pitch and the open-ratio of G_0. The line-source size is the extent of the opening in one pitch period P_0, or $L_s = P_0 \Upsilon_0$. The source coherence length l_c has to be larger or equal to P_{MPG}, the pitch of the MPG. With this constraint, for $P_{MPG} = 0.6\ \mu m$, $D_{sg} = 250\ mm$ and 40 keV, we would obtain $L_s = 12.9\ \mu m$. Since fringe patterns created by different line sources should be superposed on the detector, the pitch of the G_0 grating can be calculated as $P_0 = \frac{W'}{D_{gd}} D_{sg} = 62.5\ \mu m$, where MPG-to detector distance D_{gd} is

600 mm and the fringe period in detector W' is 150 μm in our case. This would lead to an open-ratio $\Upsilon_0 = \frac{12.9}{62.5} = 20.64\%$. This is similar to that used in TLXI systems [34, 35, 38].

For MPG with larger pitches, all else being equal, the required coherence length l_c will be larger and line-source L_s has to be smaller and the open ratio of G_0 has to be lowered. For 1 μm pitch MPG, L_s has to be reduced to 7.7 μm and the open-ratio Υ_0 decreases to 12.4%. These parameters are summarized in Table 2.2. We computed (via SRDI) the fringe pattern with a line-source for the 0.6 μm P_{MPG} case with $L_s = 12.9\ \mu m$ and show in the results section.

Table 2.2. Summarized parameters designed for spatial coherence requirements.

Geometry	Design Energy	Fringe Period	MPG Pitch (μm)	Source Grating G_0	
				Pitch P_0 (μm)	Open-ratio Υ_0 (%)
$D_{sg} = 250\ mm$ $D_{gd} = 600\ mm$	$40\ keV$	$W' = 150\ \mu m$	0.6	62.5	20.64
			1	62.5	12.4

Since the source grating G_0 decouples the focal spot size of X-ray tube and requirements of spatial coherence, the resolution of fringes is independent of the imaging spatial resolution [34, 35]. The spatial resolution or the focal spot blur for scanning object is still determined by the focal spot size of X-ray tube and the geometry of source, object and detector as in non-interferometric Breast CT. Figure 2.9 illustrates that source grating decouple the fringe formation from X-ray focal for spot, by creating a series of mutually incoherent virtual small line sources for the phase grating [34, 35]. The small line source in each source grating pitch (red, blue and green beam showed in Figure 2.9) independently work each as a coherent X-ray source and produce a fringe pattern at detector, like the fringe pattern in red, blue and green color in Figure 2.9. Since all the fringe

patterns are produced with the same geometric magnification factor, all the fringes patterns have the same period, but with different off-axis translation at transverse (detector) plane. In general, since these sources are mutually incoherent these patterns will superpose and will blur together and may overlap completely destructively. However, if the difference in off-axis translations of fringe patterns (red, blue, green) produced by these adjacent pitches in source grating is exactly equal to fringe period, the fringe patterns produced by adjacent pitches overlap constructively and without blurring. The period of the source grating can enable all the fringe patterns to totally "register" to maintain the fringe visibility of merged intensity pattern.

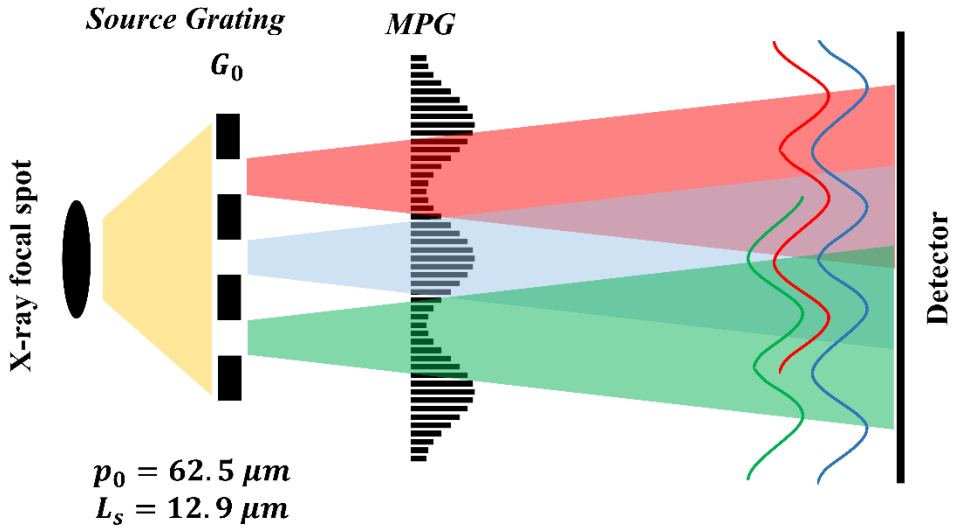

Figure 2.9. The source grating breaks a large size focal spot into a series virtual small line sources to elimination the effect of focal spot blur in fringe intensity pattern.

2.5 Phase Sensitivity and Example in Breast CT Geometry

The phase sensitivity for an interferometer is defined as

$$S = \frac{\Delta\varphi}{2\pi\alpha} \tag{6}$$

where α is the refractive angle caused from the object's differential phase shift profile and $\Delta\varphi/2\pi$ is the measured phase shift in intensity fringes, which is normalized by 2π [51]. As the

parallel beam shown in Figure 2.10, the refractive angle α from an object's differential phase shift profile in y-direction $\frac{\partial \Phi}{\partial y}$ is

$$\alpha = \frac{\lambda}{2\pi}\frac{\partial \Phi}{\partial y} \tag{7}$$

where λ is the wavelength, Φ is the phase shift profile of object and the integrated phase shift measurement

$$\varphi = S\lambda \int \left(\frac{\partial \Phi}{\partial y}\right) dy \tag{8}$$

The fringe intensity shifts Δy in the detector caused by refractive angle α is $\Delta y = D_{od} tan\, \alpha \approx \alpha D_{od}$, where D_{od} is the distance between the object and detector. Since the normalized intensity fringe phase shift $\Delta\varphi/2\pi$ can be obtained by $\Delta y/W'$, the phase sensitivity of our MPG interferometer is calculated as

$$S = \frac{D_{od}}{W'} \tag{9}$$

For the cone-beam "inverse" geometry with MPG up-stream of object ($D_{od} < D_{gd}$), following Tilman et al. [51], the fringe intensity shift Δy in the detector remains as αD_{od}. Therefore, the phase sensitivity remains the same in the inverse geometry mode with a point source. To demonstrate that the phase sensitivity of MPG is proportional to object-to-detector distance and inversely proportional to intensity fringe period, we compute the fringe patterns (via SRDI) for a ramp-shape object in a constant differential phase shift, 2π rad/mm, with different D_{od} (40-60 cm) and W' (100-200 μm) at 40 keV in cone-beam geometry. Then, the integrated phase shift measurements φ are retrieved by single-shot method without scaling by phase sensitivity. For a fixed constant $\frac{\partial \Phi}{\partial y}$, φ is proportional to phase sensitivity S for different cases of D_{od} and W'. The variation of sensitivity versus D_{od} and W' are shown in results section.

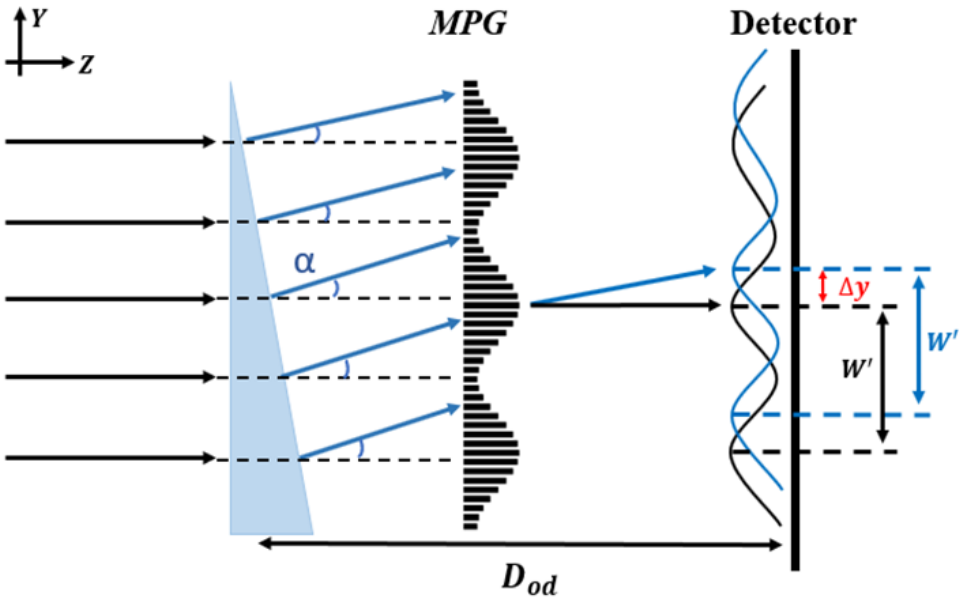

Figure 2.10. Schematic diagram of phase sensitivity in parallel beam. The refractive angle α from an object in ramp shape with a constant differential phase shift in y-direction causes the intensity fringes shift Δy in the detector. D_{od} is the distance between the object and detector. The intensity fringes are in period W'.

MPG example in Breast CT geometry: According to current clinical based BCT prototypes, the space between x-ray source and the isocenter is generally ~50 to 65 cm and the magnification factors in the range of 1.4 to 2. The circular opening on the table for hanging uncompressed breast is in ~30 cm diameter [21, 23]. The X-ray tube works in 50 to 80 kV with Al filter or 0.2 to 0.3 mm Cu filter (UC Davis) [20-23]. We refer to parameters in Table 2.1 to build up a similar geometry for MPG application in Brest CT (Figure 2.11).

In our geometry, the distance from x-ray focal spot to isocenter (the center of object) kept at 50 cm (to be at par with UC Davis system). Considering there is a small space between focal spot and x-ray tube window and installation of filter or collimator, the source grating G_0 is placed 10 cm away from the focal spot. The D_{sg} and D_{gd} keep in 25 cm and 60 cm. Consequently, for the 0.6 μm pitch MPG, to obtain 150 μm intensity fringe period at designed energy 40 keV, the setup of source grating (pitch P_0 and open ratio Υ_0) and collimator are same

to previous simulations in Part 2.4. The distance from isocenter to the detector, D_{od} is 45 cm and the magnification factor for object is 1.9. Therefore, the phase sensitivity $S = \frac{D_{od}}{W'} = \frac{45\ cm}{150\ \mu m} = 3 \times 10^3$. With the high-resolution detector, if we optionally require the focal spot blur is less than a single pixel size (50 μm), the source focal spot size is less than $\frac{50\ \mu m \times 500\ mm}{450\ mm} = 55.5\ \mu m$. Therefore, a pinhole collimator is to be placed close to the focal spot (generally 0.3 mm) to ensure a small source size.

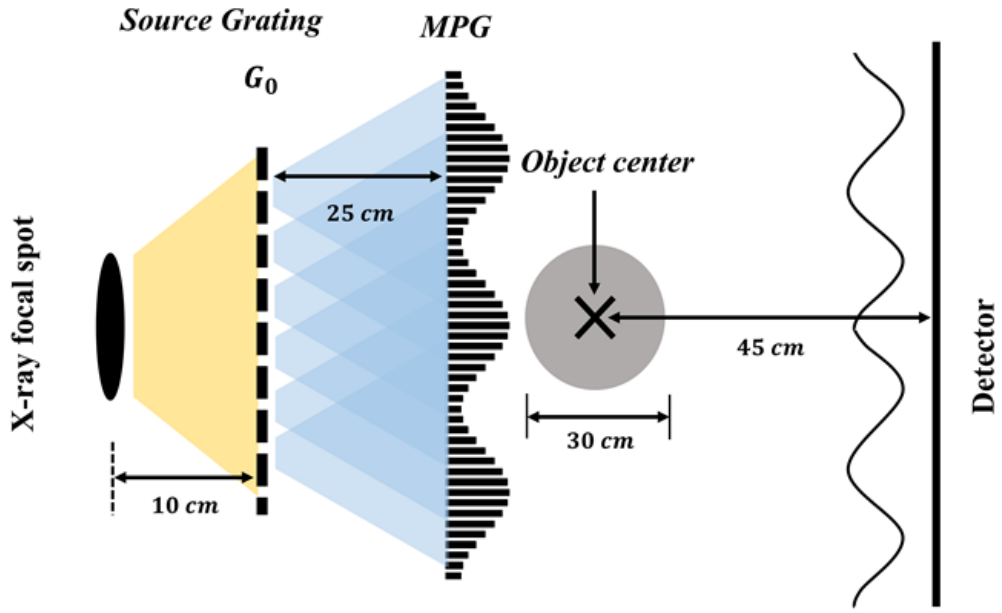

Figure 2.11. An example of MPG application in Breast CT geometry. The design energy is 40 keV and MPG parameters are 0.6 μm pitch and 45 μm W. The source grating G_0 with 62.5 μm P_0 and 20% open ratio is placed 10 cm away from focal spot. The open extent of collimator is 29 μm to limit 50 μm focal spot blur in detector. D_{sg}, D_{gd} and D_{od} are 25 cm, 60 cm and 45 cm.

2.6 Quantitative X-ray SAS with MPG Interferometry

Similar to change in a refractive index, the path change of a scattered X-ray wave causes a translation of fringe pattern in transverse plane. Different angular scattering of X-rays will shift the fringe intensity pattern by different degrees. For a specific small scattering angle, an X-ray

beam scattered by a point will distribute symmetrically in all radial directions with equal probability. And the superposition of all shifted fringe intensity patterns from each singly scattered X-ray angle is the detectable intensity pattern by interferometry. This process modulates the periodic fringe intensity pattern with local distortions of fringe visibility [52]. The degradation of fringe visibility is treated as a sign of SAS power [52-54]. Figure 2.12 illustrates the mechanism of fringe pattern modulation as a result of an X-ray beam scattered bilaterally at same angle. In Figure 2.12, comparing to the fringe intensity pattern without a point scattering (in blue) and the fringe pattern with symmetric bilateral scattering (in purple), SAS has a blurring effect on intensity pattern.

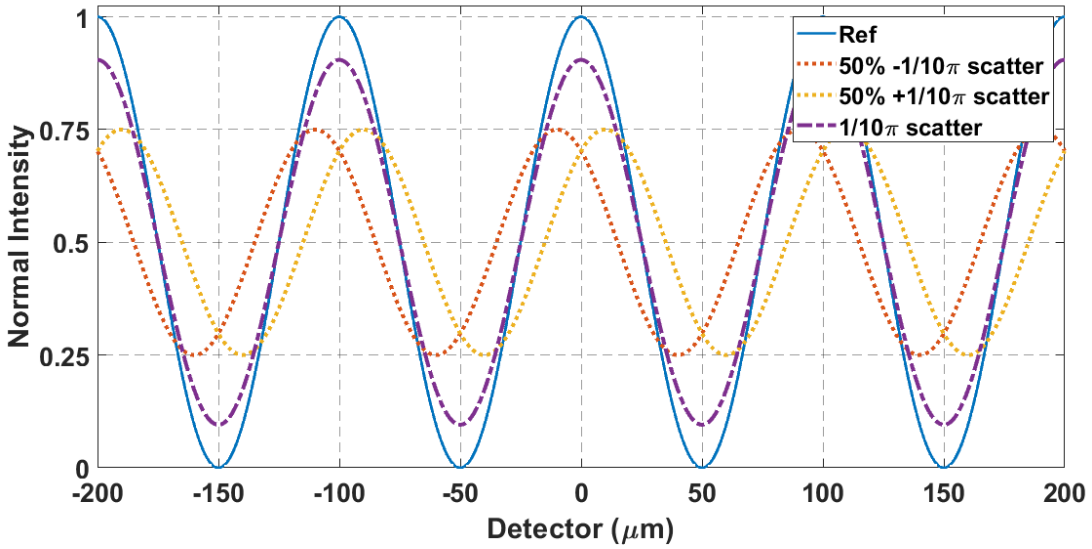

Figure 2.12. Illustration of the mechanism of fringe pattern modulation as a result of an X-ray beam scattered bilaterally at same angle. The blue is the reference without scatter. The red and yellow lines represent the intensity pattern of half X-rays scattered with ±1/10π modulation. The purple line is the fringe pattern of all scattered X-rays.

Even for a coherent (including temporal and spatial coherence) incident beam, X-rays are scattered at different small angles. Generally, the distribution of scattering angles θ_{SAS} from a point is assumed as a Gaussian distribution

$$P(\theta_{SAS}) = \frac{1}{\sigma\sqrt{2\pi}} e^{-\frac{\theta_{SAS}^2}{2\sigma^2}} \quad (10)$$

where σ^2 is the variance of the Gaussian distribution to express the divergence of incident X-ray beam.

Based on the physical model of phase sensitive imaging method built up by *Khelashvili, et al.*, σ^2 can be written as

$$\sigma^2 = \int_0^z B(z)dz = \int_0^z \left[\frac{\rho_n(z)\sigma_s(z)}{2\alpha_p}\right] dz \quad (11)$$

where ρ_n is the density of sample, σ_s is the scattering cross section and $\alpha_p$is the angular beam broadening due to a single spherical scatter event [53, 54], and$B = \frac{\rho_n(z)\sigma_s(z)}{2\alpha_p}$ represents the quantitative ratio for a point SAS. The small scattering angle θ_{SAS} can be approximated as $\theta_{SAS} \approx \tan\theta_{SAS} = \frac{x}{d}$, where x is the off-axis displacement of scattered X-ray at detector and d is the perpendicular distance from the sample to detector. Then from (10) the spatial intensity distribution of a point SAS can be written as

$$D(x) = \frac{1}{\sigma\sqrt{2\pi}} e^{-\frac{1}{2}\left(\frac{x}{\sigma d}\right)^2} \quad (12)$$

For a point SAS event, the intensity pattern with SAS modulation $I_s(x)$ can be produced by

$$I_s(x) = I(x) * D(x) \quad (13)$$

where $I(x)$ is the fringe intensity pattern without sample [54].

2.7 Single-Shot Method to Retrieve Three Contrast Modalities from Raw Acquisitions

A raw projection from interferometry system is a mix of attenuation, phase shift and small-angle scattering. Phase stepping is the generally applied data acquisition method to extract phase gradient from projections. For a TLXI, "stepping" is approached by scanning on transverse axis over at least one period of analyzer and projection at each point of scanning is acquired. For

every single pixel, there is an oscillation observed on intensities as a function of transverse scanning positions [55]. Since the phase gradient at each pixel is independent of attenuation of signals [55], the pure phase profile image can be reconstructed by simple integration. However, multiple acquisitions by scanning in steps extend the total time of exposure. And since stepping acquisition requires translating the source or grating accurately, it is sensitive to motions and mechanical stabilities [56].

Different contrast modalities modulate the fringe intensity pattern in different formats. Attenuation only reduce the intensity of fringe pattern. Differential phase shift only translates the fringe pattern. SAS just causes local visibility degradations. Based on these differences, according to Bevins et al. [44] and Takeda et al. [57], a raw projection of intensity with moiré pattern can be approximately written as

$$I(x,y) \approx I_0(x,y) + I_1(x,y)\cos\left[\frac{2\pi}{p_m}(x\cos\theta_m + y\sin\theta_m) + \phi\right] \quad (14)$$

where p_m and θ_m are period and angle of moiré pattern, I_n is the nth Fourier coefficient and ϕ is the differential phase shift due to grating and object. In the Fourier domain of a raw acquisition, the attenuation contrast concentrates in the zeroth hormonic peak, which represents I_0 term in Eq (14). The differential phase shift concentrates in the phase angle of first hormonic peak, which is located at the frequency of periodic fringes $\frac{1}{p_m}$. And the visibility reduction due to SAS represented by I_1 term in Eq (14) can be extract by $\frac{I_1}{I_0}$. Figure 2.13 is the schematic of the process of Single-shot method to retrieve each contrast modality. Three contrast modalities can be retrieved by

$$T = -\log\left(\frac{I_0}{I_1}\right) \quad (15)$$

$$DPS = \arg(I_1) \quad (16)$$

$$V_{SAS} = -\log\left(\frac{I_1}{I_0}\frac{I_{0b}}{I_{1b}}\right) \quad (17)$$

where I_0, I_1, I_{0b} and I_{1b} are magnitude of $FT^{-1}$of zeroth harmonic peak in frequency domain of projection with sample, magnitude of $FT^{-1}$of first harmonic peak in frequency domain of projection with sample, magnitude of $FT^{-1}$of zeroth harmonic peak in frequency domain of reference projection without sample and magnitude of $FT^{-1}$of first harmonic peak in frequency domain of reference projection without sample. Considering the phase sensitivity S in Eq (9) the DPS of sample is $\frac{d\Phi}{dx} = DPS/S$, and SAS distribution in in Eq (12), yields SAS of sample is $\sigma^2 = \frac{1}{2\pi^2}\left(\frac{p_m}{d}\right)^2 V_{SAS}$.

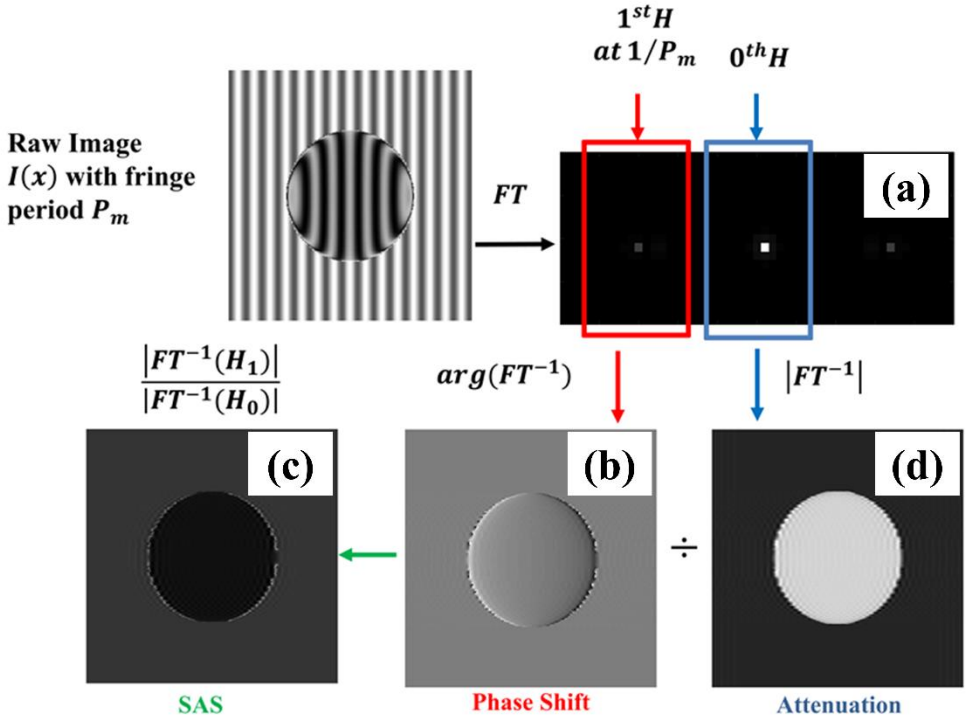

Figure 2.13. Example of single-shot retrial method. (a) Fourier transformation of a raw projection including harmonics in 0th and ±1st. (b) Phase profile. (c) Dark-field. (d) Absorption.

CHAPTER 3. RESULTS

3.1 Performance Analysis Results

3.1.1 Parallel Source, Intensity Carpet and Fringe Analysis

The intensity carpet is shown in Figure. 3.1 for 1 μm and 0.6 μm pitch of the MPG respectively for $W = 100\ \mu m$. The fringe peak-to-peak follows the peak-to-peak of the slow varying modulation in the grating (that is, fringe period $W' = 100\ \mu m$ here). This is as expected from the source being parallel and the concepts outlined in Figure 2.6 to 2.7.

Figure. 3.2 (a) shows that the fringe visibilities in general increase with distance and decrease after reaching the maximum value. The lower energy, the shorter grating-to-detector distance needed to reach the maximum visibility. Figure 3.2 (b)-(c) show the fringe visibility dependence with MPG parameters modulation period W and pitch P, showing an inverse relation with both: that is, lower the W or P, higher the visibility.

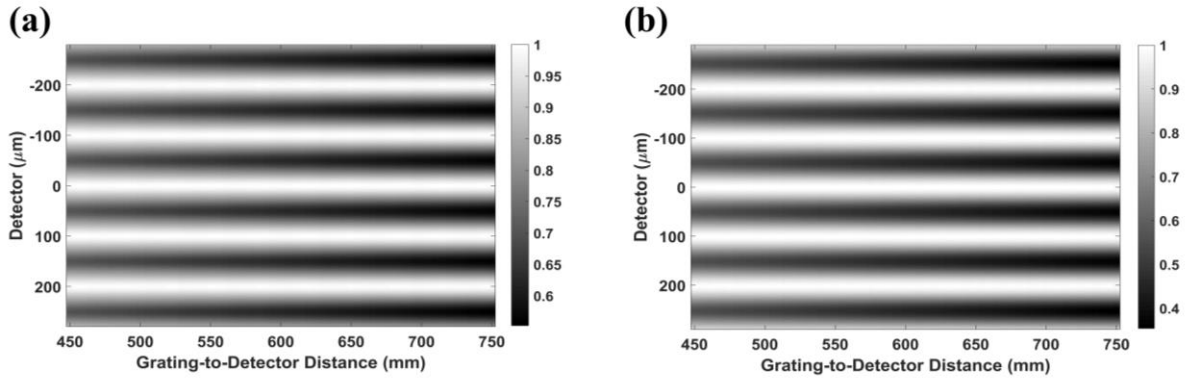

Figure 3.1. Fringe intensity carpet for parallel beam at 40 keV with 100 μm W, from 45 to 75 cm MPG-to-detector distance. (a) 0.6 μm MPG pitch. (b) 1.0 μm MPG pitch.

3.1.2 Monoenergetic Point Source Intensity Carpet and Fringe Analysis in Spectrum

The fringe intensity carpet is re-generated for a 40 keV point source, 25 cm from the MPG (0.6 μm P, 45 μm W). The carpet for 45 to 75 cm MPG-to-detector D_{gd} distance is shown in

Figure 3.3. The fringe period W' is scaled by the geometric magnification factor, given by ratio of $\frac{Dsd}{Dsg}$. For the detector intensity at $D_{gd} = 60\ cm$, the fringe period at the detector is $W' = 150\ \mu m$.

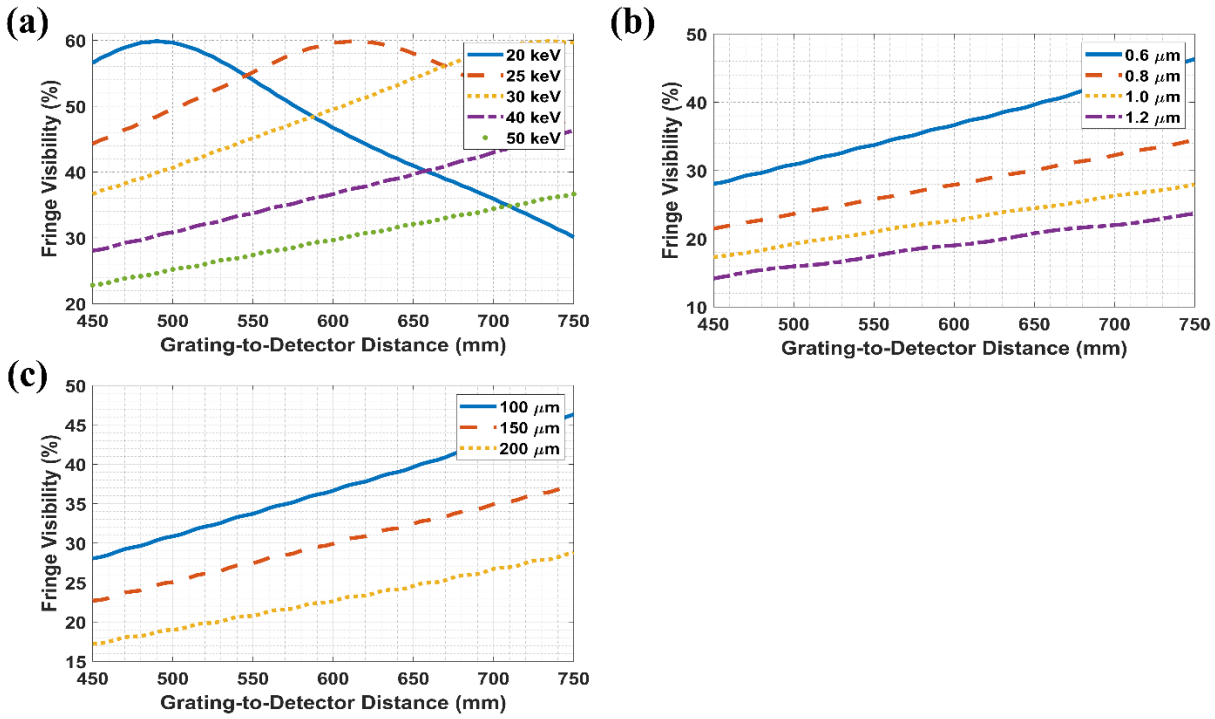

Figure 3.2. The fringe visibility analysis in parallel beam with 45 to 75 cm MPG-to-detector distance. (a) The fringe visibility with distance for different energies (in parallel beam) with 0.6 µm pitch, 100 µm W. (b) The pitch dependence of the fringe visibility at 40 keV, 100 µm W. (c) The W dependence of fringe visibility at 40 keV 0.6 µm pitch.

Figure 3.4 shows the visibility dependence on energy (without spectrum amplitude variation) for a point source, 25 cm source-to-MPG distance and 60 cm MPG-to-detector distance. The MPG phase shift is fixed at $(\pi/4, \pi)$ for the design energy 40 keV. In a result, the variation of 150 µm periodic fringe visibility is small (within 5%) in 40 ± 6 keV.

In Figure 3.5 (a) we chose a realistic BCT spectrum to investigate the degradation of fringes due to polychromatic nature of the X-ray tube beam. The spectrum is derived using 60kV, 0.2 mm Cu filter as used in UC Davis prototype for BCT[4-6]. Figure 3.5 (b) shows the fringe pattern

at pure 40 keV and with this polychromatic spectrum. We noted the fringe visibility dropped from 30.5% to about 27 %, not a significant drop in this energy range.

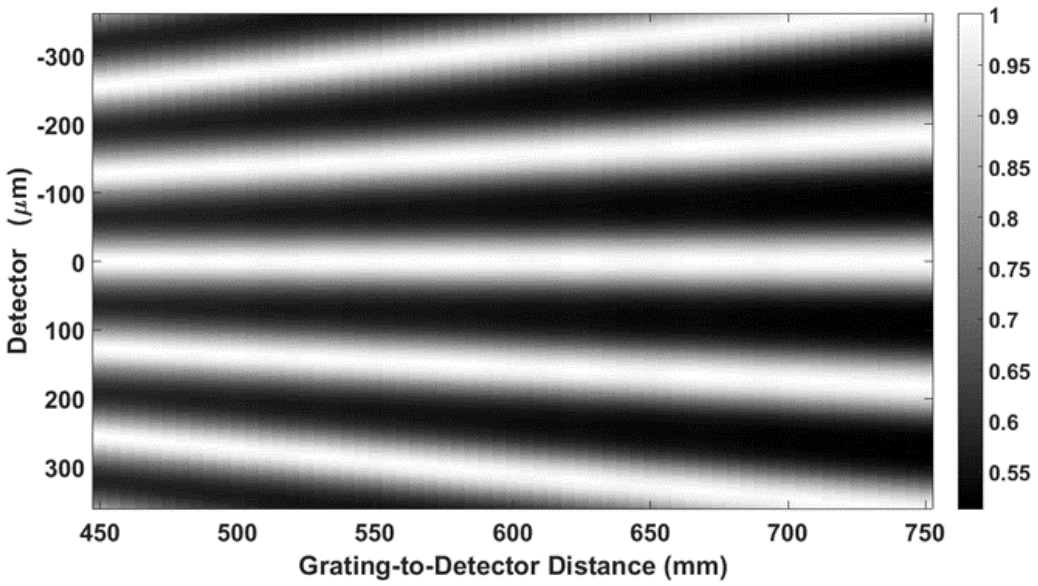

Figure 3.3. Fringe intensity carpet for a point source at 40 keV with 0.6 μm pitch in 25 cm source-to-grating distance and 45 to 75 cm MPG-to-detector distance. The fringe period is 150 μm at 60 cm MPG-to-detector distance.

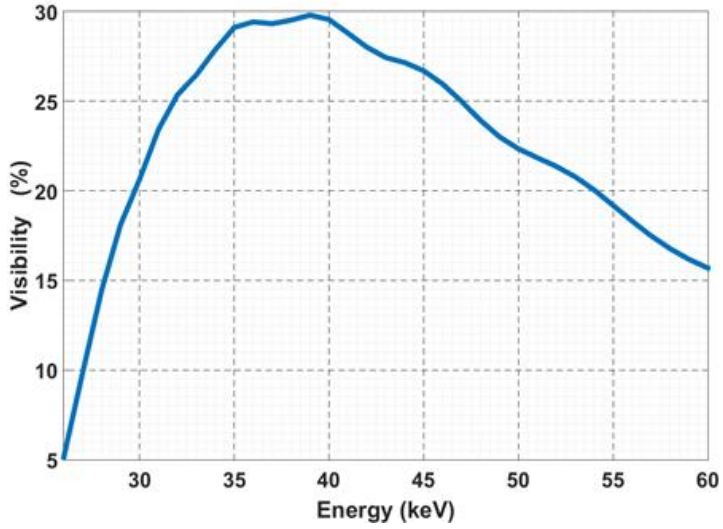

Figure 3.4. Fringe visibility dependence on energy for a point source from 26 to 60 keV with 0.6 μm pitch, in 25 cm source-to-MPG distance and 60 cm MPG-to-detector distance. The MPG phase shift is fixed at $(\pi/4\,,\pi)$ for 40 keV.

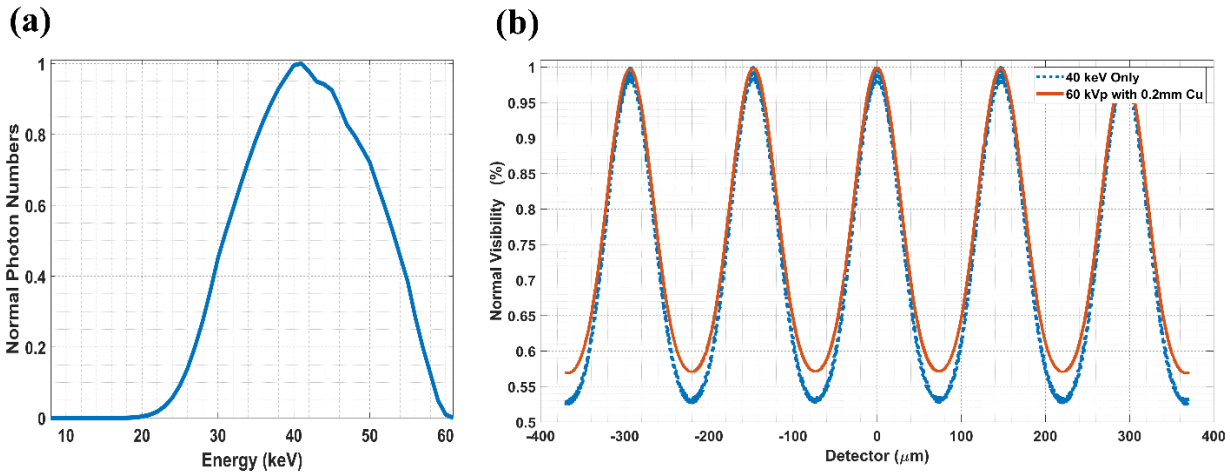

Figure 3.5. Fringe analysis in spectrum (using SRDI). (a) An example spectrum chosen for BCT with 60kV and 0.2mm Cu. It is generated by online tool "Simulation of X-ray Spectra" from Siemens Healthcare. The mean energy mode is around 41 keV. (b) The Fringe visibility (normalized) with spectrum and at monoenergetic 40keV. The visibility dropped from 30.5% to ~27%.

3.1.3 Line Source

In Figure 3.6 we generated the fringes for a line source 12.9 μm, as calculated in Methods section. This represents an opening in G_0. The source-to-MPG distance is 25 cm and the MPG-to- detector distance is 60 cm. The MPG parameters are 0.6 μm pitch and $W' = 150\ \mu m$. The fringe visibility drops slightly from 30.5% to 28.4%.

3.1.4 MPG Pitch

With the same geometry, 25 cm source-to-MPG distance and 60 cm MPG-to-detector distance and same fringe period $W' = 150\ \mu m$, we generated the fringes for 0.6 μm and 1 μm MPG pitch with corresponding coherent line source size in 12.9 μm and 7.7 μm in a Breast CT spectrum (Figure 3.5 (a)). The fringe visibility drops from 27% to 16.1%.

The results of fringe visibility analysis are summarized in Table 3.1.

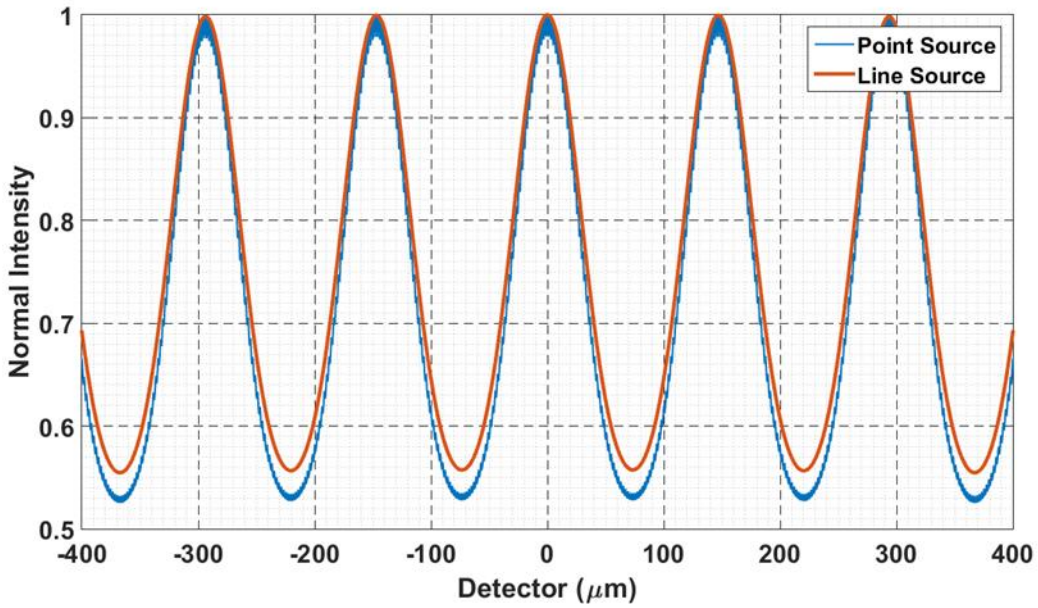

Figure 3.6. Comparison of point source and line source (using SRDI). The sources are 25cm from MPG. The MPG pitch is 0.6μm and $W' = 150$ μm. The detector is 600mm from MPG. We note a drop of fringe visibility from 30.5% to about 28.4%.

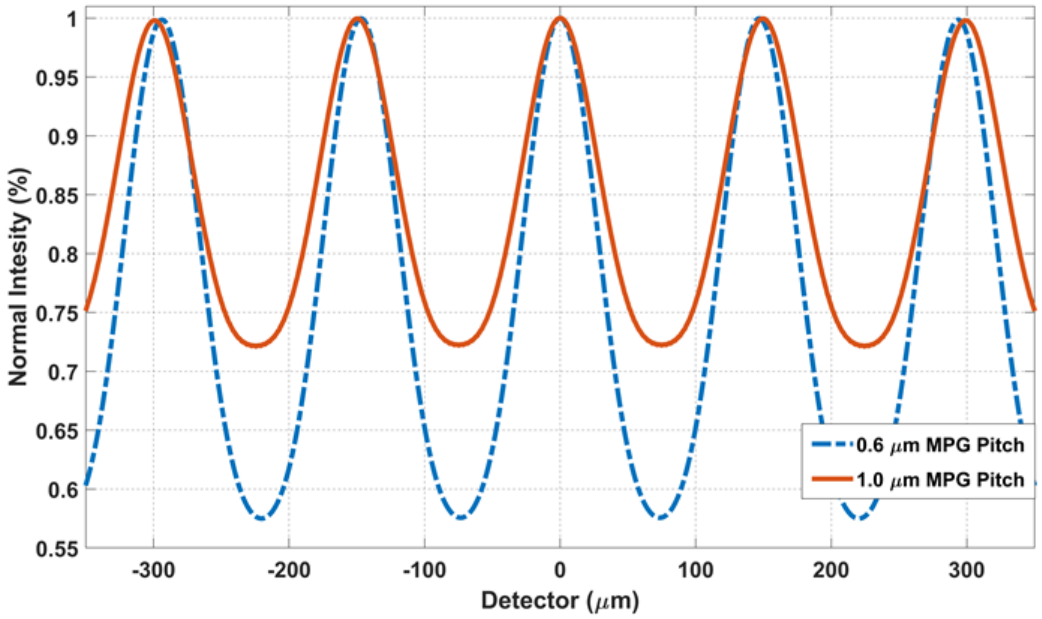

Figure 3.7. Comparison of MPG pitch (using SRDI) with spectrum and line source. The sources are 25 cm from MPG and $W' = 150\ \mu m$. The detector is 60 cm from MPG. We note a drop of fringe visibility from 27% to 16.1%.

Table 3.1. Summarized fringe visibilities for different simulations.

Source	Fringe Period in Detector	MPG Pitch (μm)	Energy	Visibility (%)
Point Source	$W' = 150\ \mu m$	0.6	$40\ keV$	30.5
			Spectrum with 60 kVp and 0.2 $mm\ Cu$	27
Line Source			$40\ keV$	28.4
			Spectrum with 60 kVp and 0.2 $mm\ Cu$	27
		1.0		16.1

3.2 Phase Sensitivity Results

Figure 3.8 shows that the measurement phase profile φ is proportional to phase sensitivity $S = \frac{D_{od}}{W'}$ for a ramp shape object with $\frac{\partial \Phi}{\partial y} = 2\pi\ rads/mm$. In Figure 3.8, The measurement phase profile φ spans 500 μm in y-direction, thus the object phase profile Φ is a ramp from 0 to π. The MPG is in 0.6 μm pitch and the source-to-MPG distance is 25 cm. In Figure 3.8 (a), we retrieved φ from fringe intensities with different fringe period W' at same object-to-detector distance $D_{od} = 60\ cm$. The scaled measurement phase profile $\frac{\varphi}{\lambda D_{od}} = \frac{\Phi}{W'}$ is inverse proportional to W'. In Figure 3.8 (b), we retrieved φ from fringe intensities at different object-to-detector distance D_{od} with same fringe period $W' = 150\ \mu m$. The measurement phase profile φ is proportional to D_{od}.

We also simulated with an object in Breast CT geometry as Figure 3.9 (a) shows. The source-to-MPG distance is 25 cm, the MPG-to-detector distance is detector distance is 60 cm and the object-to-detector distance is 45 cm. And the scanning energy of a point source is 40 keV. The simulated object as Figure 3.9 (b) shows is a PMMA block of 1.4 mm width, 260 μm thickness

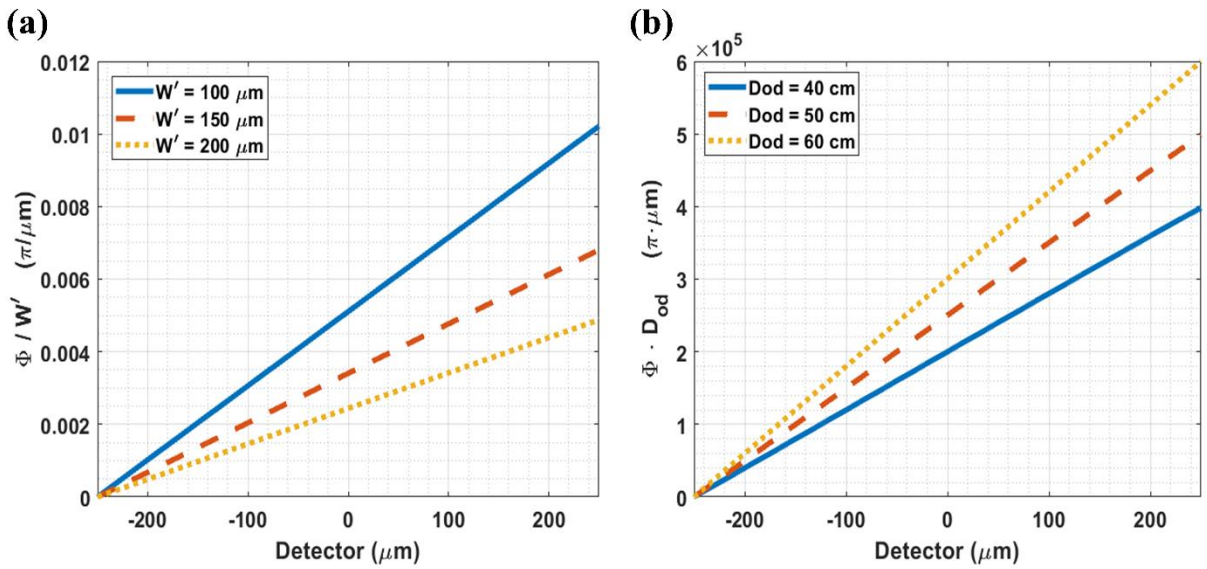

Figure 3.8. Phase sensitivity dependence on W′and D_{od} (object distance). Measured with a constant differential phase shift object and integrated, obtaining a ramp across the detector with 0 to π shift in 500 μm. (a) Phase sensitivity in units of π for different W′. The higher the W′, less the sensitivity. (b) Phase sensitivity in units of π for different object distance. Higher the object distance, better the phase sensitivity.

and corresponding 0.79π phase shift in beam propagation direction at 40 keV. A polyimide block in 0.4 mm width, 130 μm thickness and corresponding 1.6π phase shift is embedded at the center of the PMMA block. The projected phase profile of this object on the detector is retrieved by single-shot method [44] from fringes with phase sensitivity $\frac{D_{od}}{W'} = \frac{45\ cm}{150\ \mu m} = 3 \times 10^3$. Figure 3.9 (c) shows the projected phase profile of object on the detector and the retrieved phase profile from fringes.

We simulated a digital phantom composed by tissue equivalent materials scanned by MPG interferometry in the same Breast CT geometry as Figure 3.9 (a) shows. The phantom showed in Figure 3.10 (a) is a PMMA block of 1.2 mm width, 1 mm thickness and corresponding 0.6π phase shift and 2.86% absorption in beam propagation direction at 40 keV. A polycarbonate cylinder in 0.22 mm diameter and 0.78π phase shift and 2.73% absorption is inserted at the right

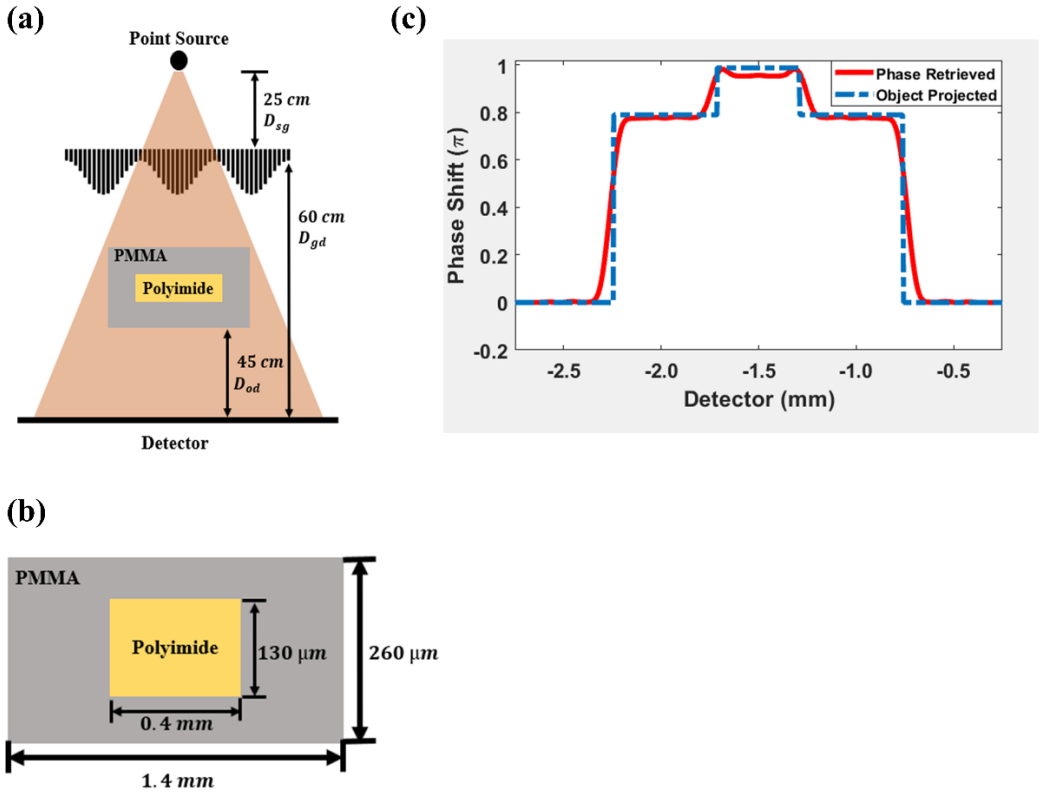

Figure 3.9. Phase profile retrieved from a simulated object projection from a point source at 40 keV. (a) The geometry of BCT and object projection. (b) The simulated object is a polyimide slab embedded in a PMMA block. (c) The retrieved phase profile from fringes and the phase projection from the simulated object on the detector.

side of the PMMA block in 0.28 mm off-center distance. There is also a water sphere in 0.32 mm diameter is embedded at the left side of the PMMA in 0.22 mm off-center distance. In the retrieved absorption contrast modality showed in Figure 3.10 (b), there is just 0.3% difference between PMMA and water. In the retrieved phase contrast modality as Figure 3.10 (c) shows, the difference is improved to 75%.

3.3 Quantitative SAS results

Different point SAS events are simulated by Gaussian distribution with different variances σ^2. As Figure 3.11 (a) shows. Since the performance of MPG interferometry in SAS is only evaluated by the scattering power in sample rather than numbers of scattering events. The

Gaussian distributions showed in Figure 3.11 (a) are normalized to a probability distribution function. The fringe intensities as reference without SAS are produced with different periods. The MPG is in 0.6 μm pitch, the source-to-MPG distance is 25 cm and the MPG-to-detector distance is 60 cm. According to Eq (13) in Section 2.6, the fringe intensity patterns with a single point SAS are generated by convolving a Gaussian distribution to the reference fringe pattern as Figure 3.11 (b) shows. The SAS profiles then are retrieved by Single-Shot methods in Figure 3.11 (c). The larger sigma, which means stronger scattering power, get higher signal strength in recovered profile.

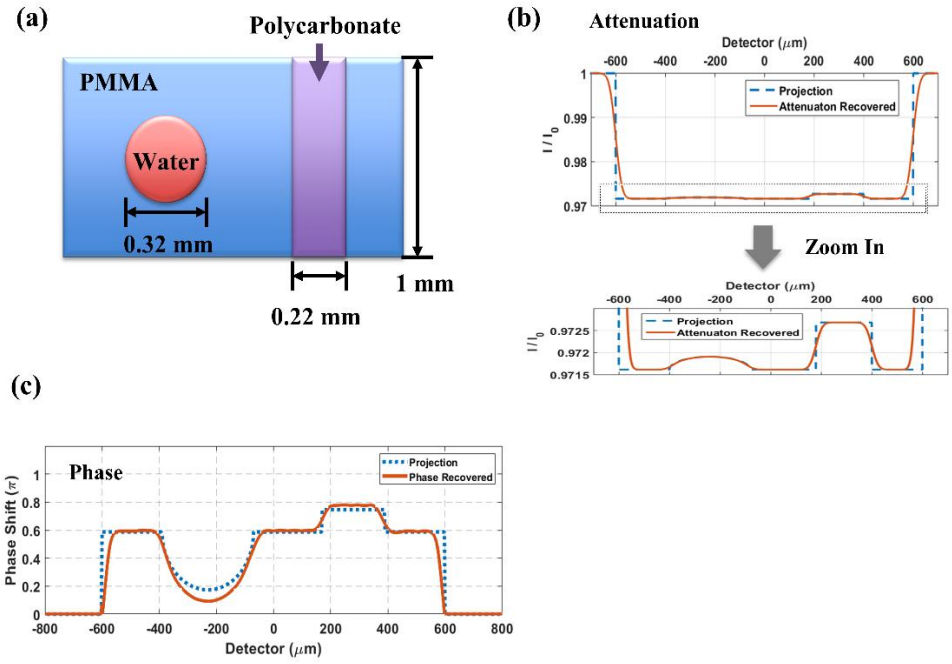

Figure 3.10. Retrieved absorption and phase projection for a tissue equivalent photom. (a) Simulated phantom and dimensions. (b) Retrieved absorption contrast of projection. (c) Retrieved phase shift contrast of projection.

Figure 3.12 shows the scattering strength from retrieved SAS profile varies with the σ^2 in Gaussian distribution with different fringe periods. The reference fringe intensity patterns are produced with 0.6 μm MPG pitch and 60 cm MPG-to-detector distance.

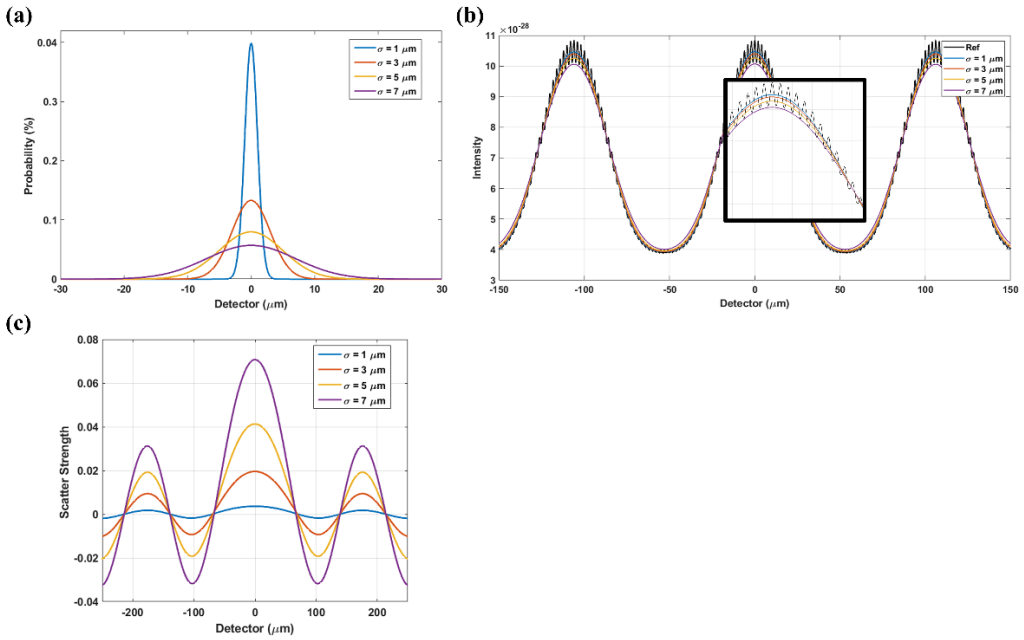

Figure 3.11. Retrieved SAS profile from angular Gaussian distribution. (a) Spatial Gaussian distributions with different scattering power. (b) Fringe intensity patterns with different single point SAS. (c) Retrieved SAS profile by single-shot method.

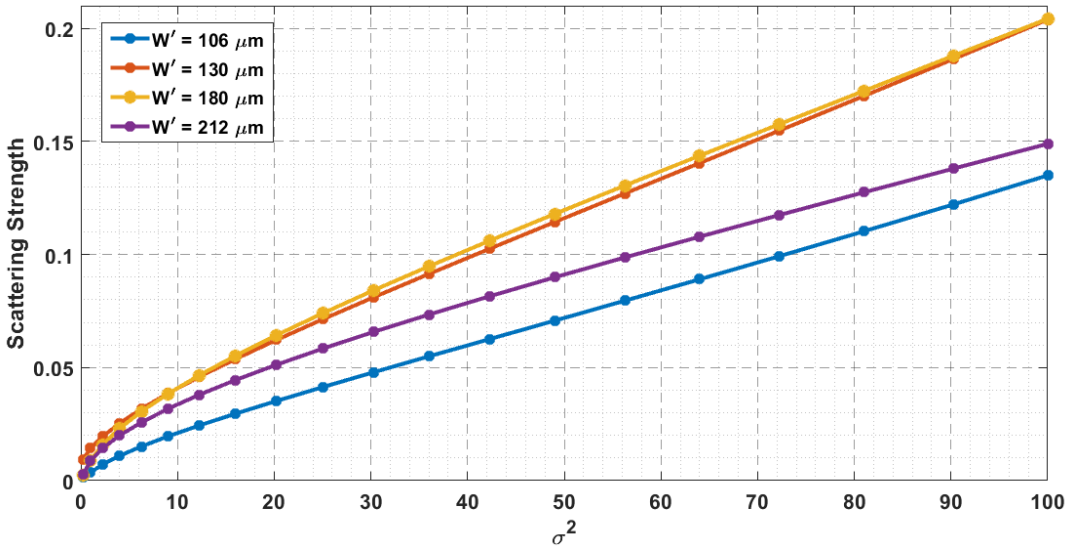

Figure 3.12. Retrieved scattering strength of single SAS Gaussian distribution vs. variance in Gaussian distribution with different fringe periods.

CHAPTER 4. DISCUSSION

We show that a spatial modulated phase grating (MPG) can be built to generate and control fringes that are visible on a standard detector (example flat-panel with 50 μm resolution) without the absorption grating (analyzer) in-between the phase-grating and detector. The period of visible fringes can be controlled by the modulation period W parameter of the grating and system magnification. The visibility at a specific geometry (given $D_{sg}$and D_{gd}) can be optimized by the height difference $(h_2 - h_1)$ of the phase-shifts of the low- and high- levels of the grating.

Our point source simulation for a common Breast CT geometry shows only a small loss of visibility from 30.5% (monochromatic) to 27% (polychromatic) visibility. Similarly using a line-source such as required for spatial coherence the fringe visibility lowered from 30.5% to 28%.

The W is nominally chosen here to be ~40 to 50 μm, which yields a fringe period of ~150 to 300 μm at detector (via magnification) which can be resolved with a 50 μm detector (such as used in the TLXI system [38]). But in fact, there are other higher resolution CCD detectors as low as ~25 μm can be potentially used for Breast CT [35, 38]. Note, provided the period is resolvable with a small enough detector resolution, a smaller W' (i.e. W for same geometry) is preferred. A smaller period yields higher visibility, higher phase sensitivity *and* provides better resolution of phase-image recovery if single-shot Fourier method [44] is used. From spatial coherence point of view as well, smaller W is preferred. For example, with spatial coherence $l_c \approx P$ is preferred. For example, with spatial coherence $l_c \approx P$, and fixed $L_s = \frac{\lambda D_{sg}}{lc} = P_0 \Upsilon_0$. fixed, lowering the W' (i.e. W for same geometry) will lower the P_0. the pitch of the G_0 grating (which is proportional to W'), thereby increasing the open-ratio Υ_0.

Note our main objective with this system is to deliver the same SNR for the attenuation image for the Breast CT acquisition, so that the MPG-Breast CT system do not degrade the tried-and-

tested attenuation images of standard Breast CT systems. On top of similar quality attenuation images, the MPG Breast CT will provide phase and scatter images. Not having the X-ray absorbing analyzer, for similar dose to the patient fluence is improved by a factor approximately 2 times with respect to clinical TLXI [38].

Since the modulated phase grating is nearly transparent to X-rays, were-iterate that the attenuation image sensitivity will be preserved with respect to the Breast CT. Not having the analyzer further reduces the system cost compared to TLXI. The cost of making our grating is largely dependent on the pitch and size. A 0.6 μm – 1 μm pitch is adequate for Breast CT operating energies. These pitch values are well within a reasonable range of manufacturing cost for X-ray phase gratings.

It is important to note that the G_0 decouples the X-ray tube source from the fringe formation [34, 35]. The focal spot of the X-ray tube will not affect the fringes resolution directly if there is a source coherence grating G_0 [35]. As far as fringe-formation is concerned we have series of small mutually incoherent "line-sources" determined by G_0 open ratio, forming registered fringes [34, 35].

However, it is also important to note that focal spot blur of the X-ray tube source affects the object similarly as in non-interferometric X-ray imaging [4-9]. With 1.5-2 magnification in our system and 0.3 mm source spot size, the effect of the focal spot on the detector is similar to another Breast CT systems [20-25].

To reduce the effective focal spot blur, a pinhole collimator may potentially be used (optionally). For our geometry, for focal spot size of nominally 0.3 mm, a 55 μm pinhole aperture will reduce the focal spot blur to under 50 μm pixel size. With the similar mA as in conventional imaging, this will increase typical Breast CT imaging times from a few seconds to few minutes.

A breast-holder may be used for imaging to reduce motion[59]. Another option is a microfocus X-ray tube with about 50 μm spot-size as has been used for Breast CT (e.g. University of Naples system [60-62]). Due to smaller allowable maximum currents, using microfocus X-ray will increase the imaging times making breast-holder essential.

If a lower resolution detector is used, the fringe period may need to be increased for adequate sampling. This can be achieved a few ways. Keeping the distance from source to grating constant, increasing the distance from grating to detector would increase the fringe period via magnification (and visibility). However, typically there are clinical limits of space in a hospital setting. Another option is to use an MPG with higher W to obtain larger fringe period in clinical compatible source to detector distance.

The analyzer double functions as a scatter grid [63]. However, in conventional Breast CT and mammography, the scatter grid not only absorbs fluence, it requires careful alignment, failing which there are image artifacts leading to repeat scans [64]. Hence the current trend in Breast CT or Mammogram is to perform grid-less scatter correction algorithms which produces equivalent image quality [65-68]. In fact, for mammography, the scatter correction algorithm from Siemens, Inc is now FDA approved and used in the clinic [69]. Similar to the grid in the mammogram or CT, the analyzer absorbs fluence and careful alignment is an issue. Another consideration is that to the relatively large magnification due to central placement of object, Breast CT the scatter effects are lower [20]. In the future, we will estimate the effect of Compton scatter and build an iterative scatter correction algorithm for our system. This could be each-projection based like in mammography [66, 67] or in 3-D object space as in Breast CT [68]. Fast Monte-Carlo methods maybe used to expedite the algorithm as done for Mammography or Beast CT [67, 68, 70].

We are in communication with Microworks GmbH, Germany [71] to build preliminary MPG gratings suitable for breast imaging. In the future we anticipate building a prototype by modifying existing TLXI systems in Pennington Biomedical Research Center, LSU and at the synchrotron source at Louisiana State University Center for Advanced Microstructures and Devices (CAMD).

CHAPTER 5. CONCLUSION AND FUTURE WORK

5.1 Conclusion

We demonstrated a novel analyzer-less X-ray interferometer, with a spatial sinusoid modulated phase-grating (MPG). We showed 27% fringe visibility with total detector-to-source distance at 95 cm, which is clinically realistic. Our system was able to deliver the attenuation image without dose or fluence detriment compared to conventional Breast CT, and also produced phase and scatter images within the same acquisition.

The MPG interferometry is a clinically compatible method. It is suitable for implementation in the same footprint as current Breast CT prototypes, including geometry, X-ray source and detector. The MPG interferometer components can be easily integrated into a clinical Breast CT system. Only two gratings, source grating and MPG, are necessary to be added onto the rotating gantry.

Multiple contrast Breast CT by MPG interferometry simultaneously provides three contrast modalities, absorption, phase shift and SAS. Comparing to attenuation-only Breast CT, the other two modalities provide additional complementary information, including improved soft tissue contrast and enhanced appearance of microcalcifications, which can presumably aid diagnostic co-interpretation of the three types of images. At the same time, microcalcification clusters in breast tumor are also detectable. Consequently, the diagnostic sensitivity of breast imaging can be boosted.

5.2 Future Work

Optics method of Sommerfeld-Rayleigh diffraction integral treats X-rays as an electromagnetic wave to simulate interference profiles which encode attenuation, differential phase shift and dark field contrast. However, due to X-ray photon wave-particle duality, the

effects of photon interactions in sample, such as photoelectric absorption, Compton scatter and Rayleigh scatter, are neglected in simulations of optics method. Moreover, SAXS induced dark field contrast relies on coherent scattering processes. And interference fringe visibility is sensitive to X-ray beam coherence which can be reduced by photon inelastic scattering. MC method models each individual particle path through photon interactions probabilities determined by scattering and absorption cross sections. At the same time, the entrance/patient doses of MPG interferometry coupled Breast CT are possibly estimated. To quantify sensitivities of phase shift and SAXS, samples of different materials with specific micro-structures and scattering cross sections will be simulated in MC part. The entrance skin dose can be evaluated in MC part at the same time.

REFERENCES

[1] Rosen, PP. *Rosen's Breast Pathology*. 2nd ed. Philadelphia, PA: Lippincott Williams & Wilkins; 2001.

[2] American Joint Committee on Cancer. Breast. In: *AJCC Cancer Staging Manual*. 8th ed. New York, NY: Springer; 2017:589.

[3] Van Zee KJ., White J, Morrow M, Harris JR. Chapter 23: Ductal carcinoma in situ and microinvasive carcinoma. In: Harris JR, Lippman ME, Morrow M, Osborne CK, eds. *Diseases of the Breast*. 5th ed. Philadelphia, PA: Lippincott-Williams & Wilkins; 2014.

[4] Dillon DA, Guidi AJ, Schnitt SJ. Ch. 25: Pathology of invasive breast cancer. In: Harris JR, Lippman ME, Morrow M, Osborne CK, eds. *Diseases of the Breast*. 5th ed. Philadelphia, PA: Lippincott-Williams & Wilkins; 2014.

[5] American Cancer Society. *Breast Cancer Facts & Figures 2019-2020*. Atlanta: American Cancer Society, Inc; 2019.

[6] Siegel RL, Miller KD, Jemal A. Cancer statistics, 2020. *CA A Cancer J Clin*. 2020; 70:7-30.

[7] DeSantis CE, Ma J, Gaudet MM, et al. Breast cancer statistics, 2019. *CA A Cancer J Clin*. 2019; 69: 438-451.

[8] Mariotto AB, Etzioni R, Hurlbert M, Penberthy L, Mayer M. Estimation of the number of women living with metastatic breast cancer in the United States. *Cancer Epidemiol Biomarkers Prev*. 2017; 26:809-815.

[9] Howlader N, Noone AM, Krapcho M, et al. SEER Cancer Statistics Review, 1975-2016, National Cancer Institute. Bethesda, MD, https://seer.cancer.gov/csr/1975_2016/, based on November 2018 SEER data submission, posted to the SEER web site, April 2019.

[10] Bevers TB, Anderson BO, Bonaccio E, et al. NCCN clinical practice guidelines in oncology: Breast cancer screening and diagnosis. *Journal of the National Comprehensive Cancer Network*. 2009; 7:1060–1096.

[11] Gajdos C, Ian Tartter P, Bleiweiss IJ, et al. Mammographic Appearance of Nonpalpable Breast Cancer Reflects Pathologic Characteristics. *Annals of Surgery*. 2002; 235(2):246-251.

[12] Pinsky RW, Helvie MA. Mammographic Breast Density: Effect on Imaging and Breast Cancer Risk. *Journal of the National Comprehensive Cancer Network*. 2010; 8(10):1157-1165.

[13] Schrading S, Kuhl CK. Mammographic, US, and MR Imaging Phenotypes of Familial Breast Cancer. *Radiology*. 2008; 246(1):58-70.

[14] Tilanus-Linthorst M, Verhoog L, Obdeijn I-M, et al. A BRCA1/2 mutation, high breast density and prominent pushing margins of a tumor independently contribute to a frequent false-negative mammography. *International Journal of Cancer*. 2002; 102(1):91-95.

[15] ACR BI-RADS. *Atlas Breast Imaging and Reporting Data System*. Reston, VA: American College of Radiology; 2013.

[16] Lee CH, Weinreb JC. The use of magnetic resonance imaging in breast cancer screening. *Journal of the American College of Radiology*. 2004; 1(3):176-182.

[17] Sardanelli F, Giuseppetti GM, Panizza P, et al. Sensitivity of MRI Versus Mammography for Detecting Foci of Multifocal, Multicentric Breast Cancer in Fatty and Dense Breasts Using the Whole-Breast Pathologic Examination as a Gold Standard. *American Journal of Roentgenology*. 2004; 183(4):1149-1157.

[18] Scherer KH. Screening Value of Phase-Contrast Mammography. In: Scherer KH, ed. *Grating-Based X-Ray Phase-Contrast Mammography*. Springer, Cham: Springer Theses (Recognizing Outstanding Ph.D. Research); 2016.

[19] Makeev A, Glick SJ. Low-Dose Contrast-Enhanced Breast CT Using Spectral Shaping Filters: An Experimental Study. *IEEE Transactions on Medical Imaging*. 2017; 36(12):2417-2423.

[20] Sarno A, Mettivier G, Russo P. Dedicated breast computed tomography: Basic aspects. *Medical Physics*. 2015: 42:2786-2804.

[21] Kwan AL, Boone JM, Yang K, Huang SY. Evaluation of the spatial resolution characteristics of a cone-beam breast CT scanner. *Medical Physics*. 2017; 34(1):275–281.

[22] Gazi PM, Yang K, Burkett GW Jr, Aminololama-Shakeri S, Seibert JA, Boone JM. Evolution of spatial resolution in breast CT at UC Davis. *Medical Physics*. 2015; 42(4):1973–1981.

[23] O'Connell A, Conover DL, Zhang Y, et al. Cone-beam CT for breast imaging: Radiation dose, breast coverage, and image quality. *American Journal of Roentgenology*. 2010; 195(2), 496–509.

[24] KONING BREAST CT (MODEL CBCT1000): PMA Number P130025. *US Food and Drug Administration*. 2015. https://www.accessdata.fda.gov/scripts/cdrh/cfdocs/cfpma/pma.cfm?id=P130025

[25] Cole EB, Campbell AS, Vedantham S, Pisano ED, Karellas A. Clinical Performance of Dedicated Breast Computed Tomography in Comparison to Diagnostic Digital Mammography. *101st Scientific Assembly and Annual Meeting of the Radiological Society of North America*. 2015.

[26] Chen B, Ning R. Cone-beam volume CT breast imaging: feasibility study. *Medical Physics*. 2002; 29(5):755-770.

[27] Glick SJ, Vedantham S, Karellas A. Investigation of optimal kVp settings for CT mammography using a flat-panel imager. *Proc. SPIE 4682, Medical Imaging 2002: Physics of Medical Imaging*. 3 May, 2002.

[28] Prionas ND, Huang SY, Boone JM. Experimentally determined spectral optimization for dedicated breast computed tomography. *Medical Physics*. 2011; 38(2):646–655.

[29] Bushberg JR, Seibert Edwin JA, Leidholdt M, Jr, Boone JM. *The essential physics of medical imaing*. Philadelphia, PA: Lippincott Wilkiams & Wilkins; 2001.

[30] Momose A. Recent Advances in X-ray Phase Imaging. *Japanese Journal of Applied Physics*. 2005; 44(9A):6355-6367.

[31] Glatter O, Kratky O, eds. *Small Angle X-ray Scattering*. New York: Academic Press; 1982.

[32] Chen GH, Bevins N, Zambelli J, Qi Z. Small-angle scattering computed tomography (SAS-CT) using a Talbot-Lau interferometerand a rotating anode x-ray tube:theory and experiments. *Opt Express*. 2010; 18(12):12960–12970.

[33] Momose A, Kawamoto S, Koyama I, Hamaishi Y, Takai K, Suzuki Y. Demonstration of X-ray Talbot-Lau Interferometry. *Japanese Journal of Applied Physics*. 2003; 42:866-868.

[34] Pfeiffer F, Weitkamp T, Bunk O, David C. Phase retrieval and differential phase-contrast imaging with low-brilliance X-ray sources. *Nature Physics*. 2006; 2(4):258-261.

[35] Weitkamp T, David C, Kottler C, Bunk O, Pfeiffer F. Tomography with grating interferometers at low-brilliance sources. *Proc. SPIE 6318, Developments in X-Ray Tomography V, 63180S*. 7 September 2006.

[36] Miao H, Panna A, Gomella AA, et al. A universal moiré effect and application in X-ray phase-contrast imaging. *Nature Physics*. 2016; 12(9):830-834.

[37] Miao H, Gomella AA, Harmon KJ, et al. Enhancing Tabletop X-Ray Phase Contrast Imaging with Nano-Fabrication. *Scientific Reports*. 2015; 5:13581.

[38] Koehler T, Daerr H, Martens G, et al. Slit-scanning differential x-ray phase-contrast mammography: Proof-of-concept experimental studies. *Medical Physics*. 2015; 42(4):1959-1965.

[39] Scherer K, Birnbacher L, Chabior M, et al. Bi-directional x-ray phase-contrast mammography. *PLoS One*. 2014; 9(5):e93502.

[40] Stampanoni M, Wang Z, Thüring T, et al. The First Analysis and Clinical Evaluation of Native Breast Tissue Using Differential Phase-Contrast Mammography. *Investigative Radiology*. 2011; 46(12):801–806.

[41] Hauser N, Wang Z, Kubik-Huch RA, et al. A study on mastectomy samples to evaluate breast imaging quality and potential clinical relevance of differential phase contrast mammography. *Investigative Radiology*. 2014; 49:131–137.

[42] Wang Z, Hauser N, Singer G, et al. Non-invasive classification of microcalcifications with phase-contrast X-ray mammography. *Nature* Communications. 2014; 5:3797.

[43] Li K, Ge Y, Garrett J, Bevins N, Zambelli J, Chen GH. Grating-based phase contrast tomosynthesis imaging: proof-of-concept experimental studies. *Medical Physics*. 2014; 41(1):011903.

[44] Bevins N, Zambelli J, Li K, Qi Z, Chen GH. Multicontrast x-ray computed tomography imaging using Talbot-Lau interferometry without phase stepping. *Medical Physics*. 2012; 39: 424-428.

[45] Goodman J. *Introduction to Fourier Optics*. 2nd ed. McGraw Hill; 1988.

[46] Born M, Wolf E. *Principles of Optics*. Pergamon Press Ltd; 1970.

[47] Dey J, Xu J, Ham K, Bhusal NP, Singh V. A Novel Phase Contrast X-ray System. *2017 IEEE Nuclear Science Symposium and Medical Imaging Conference (NSS/MIC)*. 2017; 1-4.

[48] Xu J, Dey J, Ham K, Bhusal NP, Butler LG. Two-dimensional single grating phase contrast system. *Proc. SPIE 10573, Medical Imaging 2018: Physics of Medical Imaging*, 1057323. 9 March 2018.

[49] Yaroshenko A, Bech M, Potdevin G, et al. Non-binary phase gratings for x-ray imaging with a compact Talbot interferometer. *Optics Express*. 2014; 22(1):547-556.

[50] Wang Z, Zhu P, Huang W, et al. Analysis of polychromaticity effects in X-ray Talbot interferometer. *Analytical and Bioanalytical Chemistry*. 2010; 397:2137–2141.

[51] Donath T, Chabior M, Pfeiffer F, et al. Inverse geometry for grating-based x-ray phase-contrast imaging. *Journal of Applied Physics*. 2009; 106(5):054703.

[52] Strobl, M. General solution for quantitative dark-field contrast imaging with grating interferometers. *Scientific Reports*. 2015; 4:7243.

[53] Khelashvili1 G, Brankov JG, Chapman D, et al. A physical model of multiple-image radiography. *Physics in Medicine & Biology*. 2006; 51:221.

[54] Wang ZT, Kang KJ, Huang ZF, Chen ZQ. Quantitative grating-based x-ray dark-field computed tomography. *Applied Physics Letters*. 2009; 95(094105).

[55] Weitkamp T, Diaz A, David C, et al. X-ray phase imaging with a grating interferometer. *Optics Express*. 2005; 13(16):6296.

[56] Seifert M, Gallersdörfer M, Ludwig V, et al. Improved Reconstruction Technique for Moiré Imaging Using an X-Ray Phase-Contrast Talbot–Lau Interferometer. *Journal of Imaging*. 2018; 4(5):62.

[57] Takeda M, Ina H, Kobayashi S. Fourier-transform method of fringe-pattern analysis for computer-based topography and interferometry. *Journal of the Optical Society of America*. 1982; 72(1):156.

[58] Du Y, Liu X, Lei Y, Guo J, Niu H. Non-absorption grating approach for X-ray phase-contrast imaging. *Optics Express*. 2011;19(23):22669-74.

[59] Sarno A, Mettivier G, Di Lillo F, Cesarelli M, Bifulco P, Russo P. Cone-beam micro computed tomography dedicated to the breast. *Medical Engineering and Physics*. 2016; 38(12):1449-1457.

[60] Mettivier G, Russo P, Lanconelli N, Meo SL. Cone-beam breast computed tomography with a displaced flat panel detector array. *Medical Physics*. 2012; 39(5):2805–2819.

[61] Russo P, Mettivier G, Lauria A, Montesi MC. X-ray cone-beam breast computed tomography: Phantom studies. *IEEE Transactions on Nuclear Science*. 2010; 57:160–172 (2010).

[62] Mettivier G, Russo P. Cone-beam breast microCT: Image quality in propagation based phase-contrast imaging. In Poster presented at the workshop *Taking X-Ray Phase-Contrast Imaging into Mainstream Applications*, Royal Society, London, UK, 11–12 February 2013.

[63] Vedantham S, Shi L, Karellas A. Large-angle x-ray scatter in Talbot-Lau interferometry for breast imaging. *Physics in Medicine and Biology*. 2014;59(21):6387-6400.

[64] Ayyala RS, Chorlton M, Behrman RH, Kornguth PJ, Slanetz PJ. Digital mammographic artifacts on full-field systems: what are they and how do I fix them? *Radiographics: a review publication of the Radiological Society of North America*. 2008; 28:1999–2008.

[65] Monserrat T, Prieto E, Barbés B, Pina L, Elizalde A, Fernández B. Impact on dose and image quality of a software-based scatter correction in mammography. *Acta Radiologica*. 2018; 59(6):649-656.

[66] Lisson CG, Lisson CS, Kleiner S, Regier M, Beer M, Schmidt SA. Iterative scatter correction for grid-less skeletal radiography allows improved image quality equal to an anti-scatter grid in adjunct with dose reduction: a visual grading study of 20 body donors. *Acta Radiologica*. 2019;60(6):735-741.

[67] Mentrup D, Jockel S, Menser B, Neitzel U. Iterative scatter correction for grid-less bedside chest radiography: performance for a chest phantom. *Radiation Protection Dosimetry*. 2016; 169:308–312.

[68] Bertram M, Hohmann S, Wiegert J. Scatter correction for flat detector cone-beam CT based on simulated sphere models. *Medical Physics*. 2007; 34:2342.

[69] MAMMOMAT INSPIRATION WITH TOMOSYNTHESIS OPTION: PMA Number P140011. US Food and Drug Administration, 2017. https://www.accessdata.fda.gov/scripts/cdrh/cfdocs/cfpma/pma.cfm?ID=391690

[70] Jabbari K. Review of fast monte carlo codes for dose calculation in radiation therapy treatment planning. *Journal of medical signals and sensors*. 2011;1(1):73–86.

[71] Email communication, Dr. Joachim Schulz, microworks GmbH, Schnetzlerstr.9, D-76137 Karlsruhe, Germany.

VITA

Jingzhu Xu was born in China. She finished her undergraduate studies at University of Iowa, May 2014. She earned a master of science degree in Biomedical Engineering from University of Iowa in Aug 2015. In August 2015, she came to Louisiana State University to pursue graduate studies in medical physics. She is currently a candidate for the degree of Doctor of Philosophy in medical physics, which will be awarded in May 2020.